



**HAL**  
open science

# Higgs boson couplings: from Tevatron to LHC and beyond

Thibault Guillemin

► **To cite this version:**

Thibault Guillemin. Higgs boson couplings: from Tevatron to LHC and beyond. Physics [physics]. Université Grenoble Alpes, 2018. tel-01827767

**HAL Id: tel-01827767**

**<https://theses.hal.science/tel-01827767>**

Submitted on 16 Jul 2018

**HAL** is a multi-disciplinary open access archive for the deposit and dissemination of scientific research documents, whether they are published or not. The documents may come from teaching and research institutions in France or abroad, or from public or private research centers.

L'archive ouverte pluridisciplinaire **HAL**, est destinée au dépôt et à la diffusion de documents scientifiques de niveau recherche, publiés ou non, émanant des établissements d'enseignement et de recherche français ou étrangers, des laboratoires publics ou privés.

Université Grenoble Alpes

Mémoire présenté par

**Thibault Guillemin**

pour obtenir le diplôme de

**Habilitation à Diriger des Recherches**

Spécialité: Physique des Particules

# Higgs boson couplings: from Tevatron to LHC and beyond

Soutenu le 01/06/2018 devant le Jury composé de :

Pr. Gustaaf BROOIJMANS

Dr. Jean-François GRIVAZ

Pr. Christophe GROJEAN

Dr. Gautier HAMEL DE MONCHENAULT

Dr. Giovanni LAMANNA

*Rapporteur*

*Rapporteur*

*Examineur*

*Rapporteur*

*Président du Jury*



# Introduction

Already eight years have passed since the end of my PhD. Over this period, the focus of my research activities has been on the Higgs boson, discovered in 2012, from its search in the D0 experiment to the precision measurement of its properties in ATLAS, covering three different decay channels. All my diverse contributions have been built on three pillars: software, detector performance and physics analysis. A pictorial timeline, summarizing my activities along the years, is shown in Figure 1. As a guiding principle for the writing of this HDR manuscript, I have chosen to describe my most recent contributions in the three domains previously mentioned, highlighting their interplay from data taking to analysis. The covered period goes from the ATLAS Run 2 preparation (during the first LHC long shutdown) to recent Run 2 results just published.

To describe the long path from data taking to analysis, the following contributions are described in detail:

- software: development of a new analysis model for Run 2 (derivation framework)
- performance: electron and photon energy calibration
- analysis: Higgs boson coupling measurement in the diphoton channel.

Of course, all the results presented are the fruit of a huge collaboration work; my contributions are listed at the end of the relevant chapters.

My other main contributions, not discussed in this manuscript, were first done in the D0 experiment:

- Calibration of the jet energy scale
- Search for a low mass Higgs boson in the  $ZH \rightarrow \nu\bar{\nu}b\bar{b}$  channel

And later in the ATLAS experiment with LHC Run 1 and Run 2 data:

- Measurement of electron identification efficiencies at Run 1
- Measurement of the Higgs boson properties in the  $H \rightarrow ZZ^* \rightarrow 4l$  channel at Run 1
- Search for a high mass resonance in the diphoton channel (also known as the ‘750 GeV excess’).

The relevant publications for these contributions are listed in Appendix A; a snapshot of results from these publications is shown in Figure 2 (D0), Figure 3 (ATLAS Run 1) and Figure 4 (ATLAS Run 2).

This manuscript is organized as follows. The first chapter emphasises the primordial importance of the Higgs boson physics in the current high energy physics landscape. The second chapter describes the preparation of ATLAS data for analysis. The third chapter presents the recent results of the Higgs boson coupling measurement in the diphoton channel. The last chapter discusses some ideas for my future work, from short-term (LHC Run 3), to medium-term (high luminosity LHC), and up to long-term (future colliders). Both detector aspects and Higgs boson prospects are discussed.

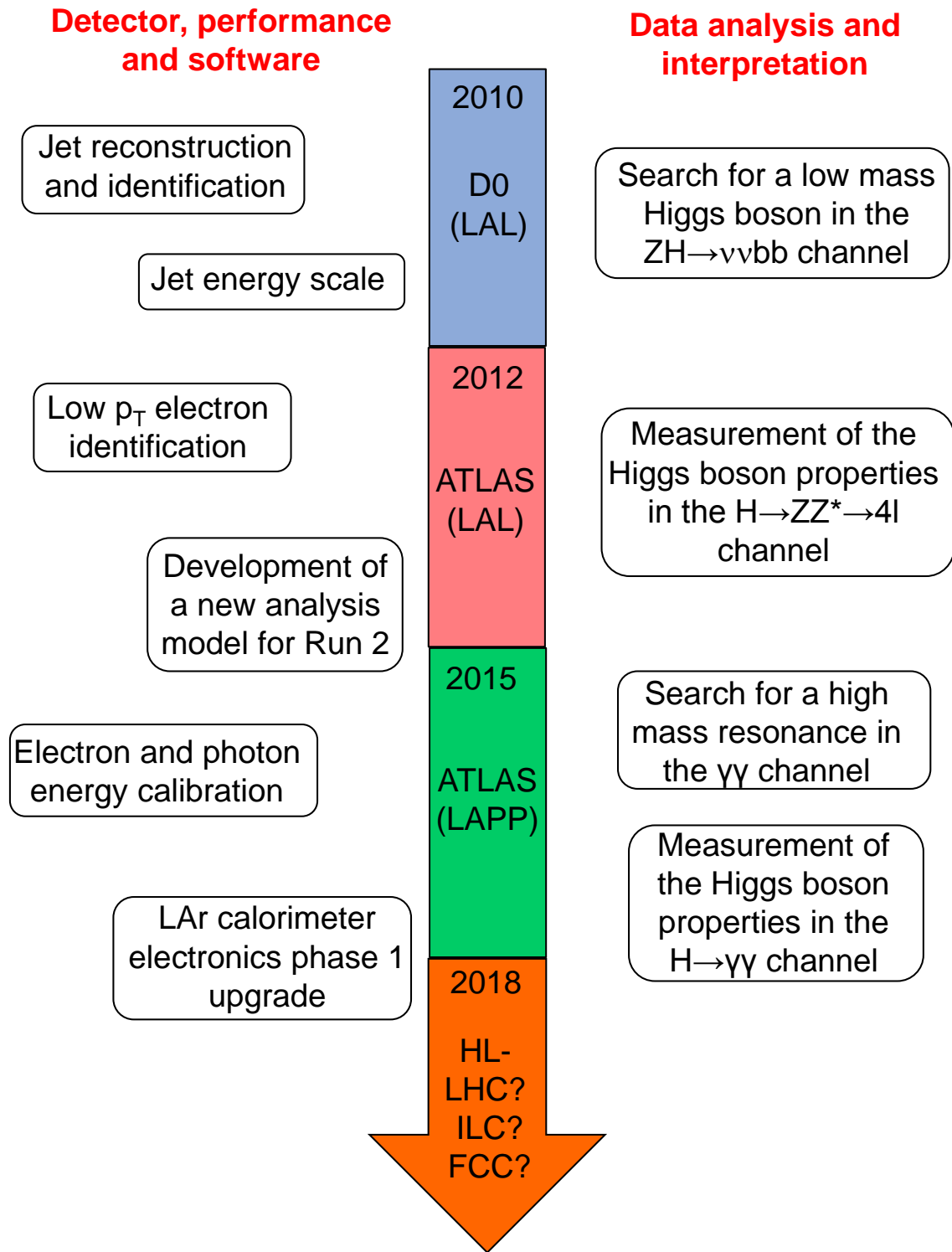


Figure 1: Timeline of my research activities since the end of my PhD.

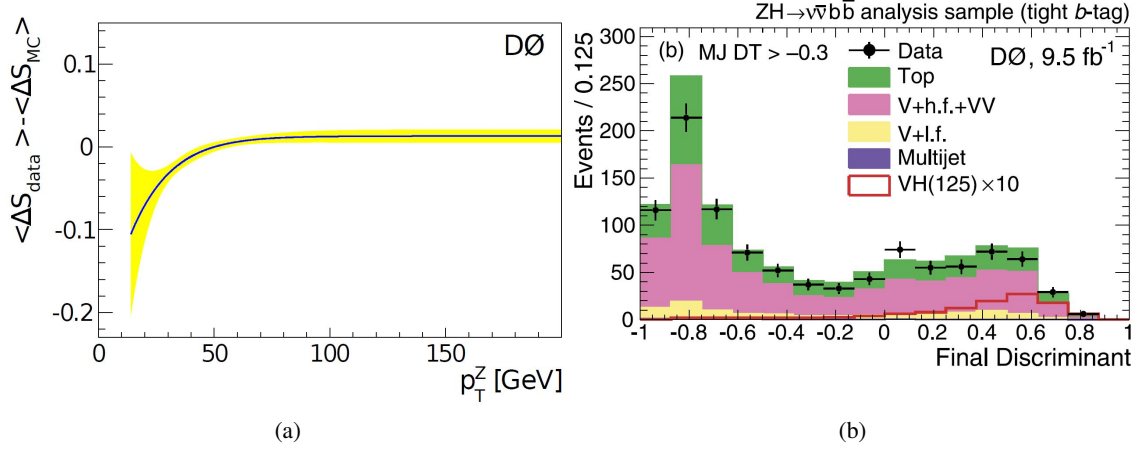


Figure 2: (a) Residual data to MC jet energy shifting as a function of  $p_{T,Z}$  in  $Z + jet$  events for central jets, determined from the transverse  $p_T$  imbalance [1]. (b) Final decision tree discriminant output for the (W/Z)H search with  $m_H = 125 \text{ GeV}$ , after a multijet veto, in the most sensitive analysis category [2].

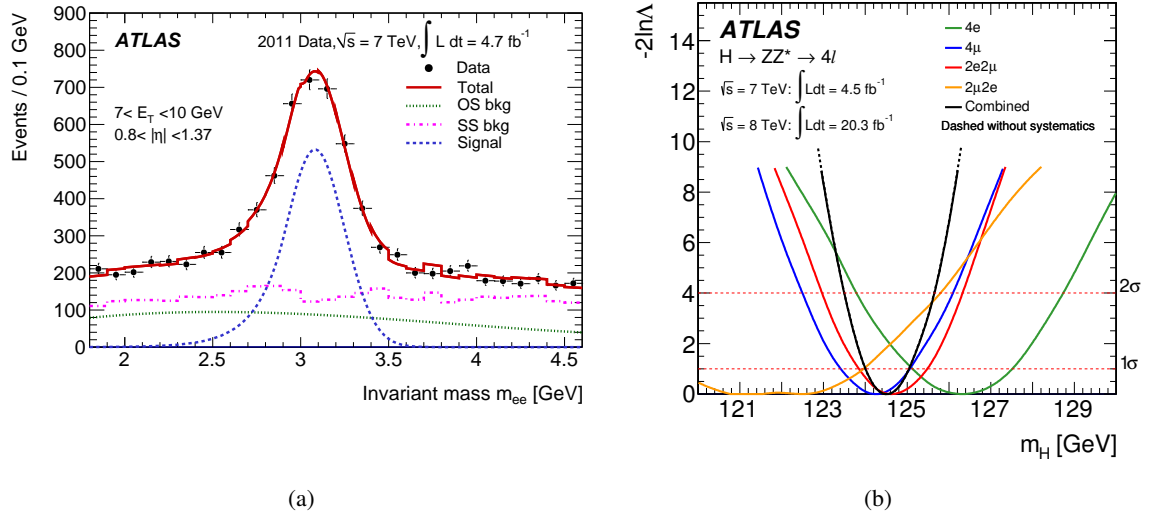


Figure 3: (a) Invariant mass distribution for the  $J/\psi \rightarrow ee$  sample in the short-lifetime range, used to measure electron identification at low  $p_T$  via a tag-and-probe technique [3]. (b) Profile likelihood as a function of  $m_H$  for the combination of all  $H \rightarrow ZZ^* \rightarrow 4l$  channels and for the individual channels, for the combined 7 TeV and 8 TeV data samples [4].

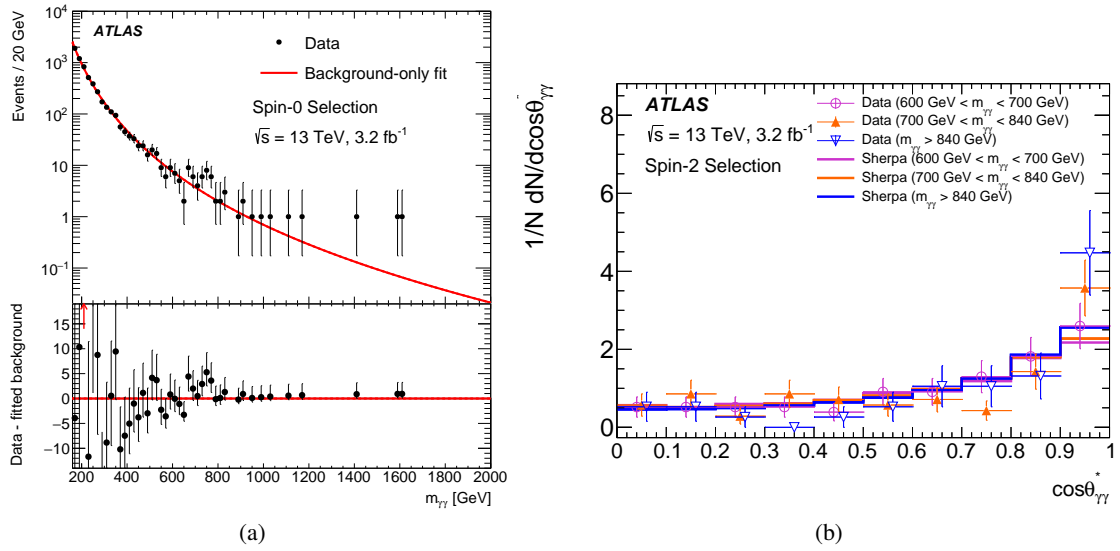


Figure 4: (a) Distribution of the invariant mass of the diphoton candidates for the selection used in the search for a spin-0 resonance with the best background-only fit [5]. The difference between the data and this fit is shown in the bottom panel. (b) Distribution of  $\cos \theta^*$  for events in the mass interval 700–840 GeV, and the regions 600–700 GeV or  $> 840$  GeV [5]. This illustrates the countless crosschecks performed in the context of the ‘750 GeV excess’.

# Contents

<b>I</b>	<b>Higgs boson physics: a brief preamble</b>	<b>10</b>
<b>I.1</b>	<b>The high energy physics landscape</b>	<b>10</b>
<b>I.2</b>	<b>Higgs boson couplings</b>	<b>11</b>
I.2.1	Production at LHC and decay	11
I.2.2	Current status	12
<b>II</b>	<b>Preparing data: the long road from detector to analysis</b>	<b>14</b>
<b>II.1</b>	<b>The ATLAS detector at LHC</b>	<b>14</b>
II.1.1	Overview of the detector	14
II.1.2	LHC Run 2 conditions in 2015 and 2016	15
<b>II.2</b>	<b>Data reconstruction, simulation and processing</b>	<b>16</b>
II.2.1	ATLAS data workflow	16
II.2.1.1	Data reconstruction	16
II.2.1.2	Monte Carlo simulation	16
II.2.2	Shaping data for analysis	17
II.2.2.1	The Run 2 analysis model	17
II.2.2.2	The derivation framework	17
II.2.3	Contributions	18
<b>II.3</b>	<b>Electron and photon energy calibration</b>	<b>19</b>
II.3.1	Overview of the calibration procedure	20
II.3.1.1	LAr cell level reconstruction	20
II.3.1.2	Cluster level calibration	21
II.3.2	Calorimeter layer intercalibration	23
II.3.2.1	Overview of the method	23
II.3.2.2	Pileup dependency	24
II.3.2.3	Pileup mitigation techniques	25
II.3.2.4	Final results	26
II.3.3	High to medium electronics gain non-linearity	27
II.3.3.1	Description of the effect and Run 1 observations	27
II.3.3.2	2017 special run analysis	27
II.3.4	Final systematic uncertainties and their correlations	29
II.3.5	Contributions	29
<b>III</b>	<b>Higgs boson coupling measurement in the diphoton channel with LHC Run 2 data</b>	<b>31</b>
<b>III.1</b>	<b>The simplified template cross section framework</b>	<b>31</b>
III.1.1	Description of the framework	31

III.1.2	Merging scheme used in the analysis	32
<b>III.2</b>	<b>Overview of the analysis</b>	<b>33</b>
III.2.1	Event simulation	33
III.2.2	Event selection	34
III.2.3	Event categorization	35
III.2.4	Signal and background modelling	35
III.2.4.1	Signal modelling	35
III.2.4.2	Background modelling	38
III.2.5	Systematic uncertainties	39
III.2.6	Statistical model	40
<b>III.3</b>	<b>Results</b>	<b>42</b>
III.3.1	Observed data	42
III.3.2	Simplified template cross sections	42
III.3.3	Other results	44
III.3.3.1	Production mode signal strengths	44
III.3.3.2	$\kappa$ -fit	45
<b>III.4</b>	<b>Contributions</b>	<b>46</b>
<b>IV</b>	<b>Higgs boson prospects with future colliders: from 2020 to 2050</b>	<b>48</b>
<b>IV.1</b>	<b>Introduction</b>	<b>48</b>
<b>IV.2</b>	<b>Future colliders at the energy frontier: what is next?</b>	<b>48</b>
IV.2.1	The high luminosity LHC program	48
IV.2.2	Linear colliders	49
IV.2.3	Circular colliders	50
IV.2.3.1	The FCC project	50
IV.2.3.2	High energy LHC	52
<b>IV.3</b>	<b>Calorimetry: from ATLAS upgrades to future experiments</b>	<b>52</b>
IV.3.1	The ATLAS LAr Phase-1 upgrade	52
IV.3.1.1	Physics requirements	52
IV.3.1.2	Overview of the upgrade system	52
IV.3.1.3	The LAr Digital Processing System	53
IV.3.1.4	Towards the production, tests, installation and commissioning	55
IV.3.2	The ATLAS LAr Phase-2 upgrade	56
IV.3.2.1	Overview of the upgrade system	56
IV.3.2.2	The LAr Signal Processors	56
IV.3.3	Beyond HL-LC	57
<b>IV.4</b>	<b>Potential for new discoveries in the Higgs boson sector</b>	<b>58</b>
IV.4.1	The precision quest	58
IV.4.2	Unexplored territories at Run 3	59
IV.4.2.1	The Higgs boson as a dark matter portal	59

IV.4.2.2	Feasibility in ATLAS	59
IV.4.3	The potential at HL-LHC	60
IV.4.4	The ultimate precision	61
IV.4.4.1	The unique prospects at an electron-positron collider	61
IV.4.4.2	The Higgs boson abundance in 100 TeV proton-proton collisions	62
IV.4.4.3	Precision comparison	63
<b>Conclusion</b>		<b>66</b>
<b>Appendix</b>		<b>70</b>
A	<b>Other contributions</b>	<b>70</b>
A.1	D0 experiment	70
A.2	ATLAS experiment	70

# Part I

## Higgs boson physics: a brief preamble

*This chapter describes very briefly the current status of the Higgs boson physics. The interplay with the main open questions of our field is first discussed. Then our current knowledge about the Higgs boson couplings is summarized.*

### I.1 The high energy physics landscape

The SM of particle physics is a theoretical triumph; it describes with an impressive accuracy all phenomena observed in experiments, in an energy range from the eV to the TeV. The experimental Higgs boson discovery, awaited for fifty years, has marked its completion. However, most of the fundamental questions of our field, on the energy and matter content of our universe, remain unsolved:

- **Naturalness**  
The radiative corrections to the Higgs mass term diverge quadratically with the renormalization scale: which mechanism does protect this divergence? Supersymmetric particles? Is the fine-tuning concept a good guiding principle?
- **Dark matter**  
Dark matter is by far the dominant mass component of our universe, but what is it made of? Do dark matter particles interact with SM particles, or are they locked in a dark sector?
- **Neutrino masses**  
Why are the neutrinos so light with respect to the other fermions? Are they their own anti-particles? Are there heavy neutrinos?
- **Matter-antimatter asymmetry**  
Which mechanism does lead to the huge dominance of matter over antimatter in our universe?
- **Quark and lepton flavour mixing**  
Is there any rationale behind the observed masses and mixings of quarks and leptons?
- **Strong CP problem**  
Why is the CP violation in QCD so small ( $\theta$  angle constrained to be smaller than  $10^{-9}$  from the electric dipole moment experimental limit)?
- **Inflation phase of the early universe**  
What is the dynamics driving the inflation of the early universe? Is there a new field required?
- **Dark energy**  
What does the dark energy consists of? Is it just vacuum energy? Is the cosmological constant interpretation correct?
- **Unification of forces**  
Do the strong, electroweak and gravitational interactions unify at some very high scale? Are there new symmetries involved?

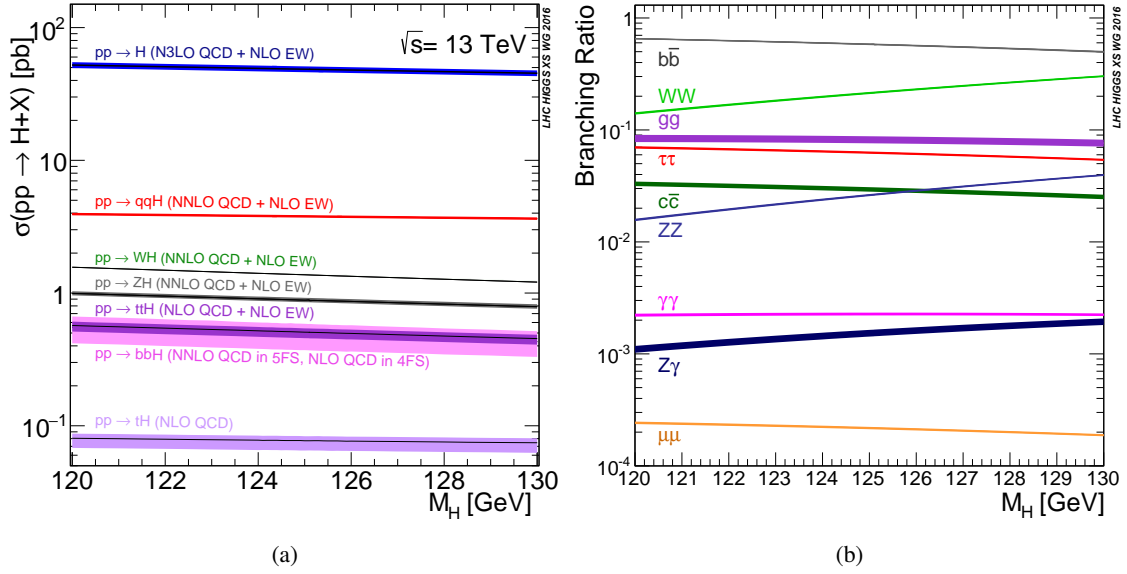


Figure 5: (a) Higgs boson production mode cross sections in proton-proton collisions at 13 TeV [6]. (b) Higgs boson branching ratios [6].

What is really striking is the possible interplay of the Higgs boson with many of these questions: the discovery of a scalar sector in the SM provides a powerful tool to probe beyond Standard Model (BSM) physics. The experimental measurements in the Higgs boson sector strongly constrain the possible models. There are essentially two approaches to study BSM physics in this sector. The first one is to consider specific scenarios, and the list here is incredibly long: two Higgs doublet models, composite Higgs models, little Higgs models, dark-matter portal models, etc. The second approach, more generic, is to look for deviations with respect the properties predicted by the SM, in particular in the measurement of the couplings with all the SM particles. This allows to probe indirectly new physics above the TeV scale (this will be discussed in Section IV.4.4.3), and the observed deviation pattern can reveal the underlying BSM scenario. This is the approach used in the work presented in this manuscript.

## I.2 Higgs boson couplings

### I.2.1 Production at LHC and decay

Once the numerical value of the Higgs boson mass is determined, all the Higgs boson production and decay rates are fully predicted in the SM. The Figure 6 (a) shows the various production mode cross sections in proton-proton collisions at 13 TeV. The dominant modes are, by decreasing order, the gluon fusion, the weak-boson fusion, the associated production with a gauge boson and the associated production with a pair of top quarks. The Figure 6 (b) shows the various branching ratios. The five main (usable) decay channels are  $bb$ ,  $WW$ ,  $\tau\tau$ ,  $ZZ$  and  $\gamma\gamma$ . Both production and decay rates are typically predicted at an accuracy level of 5% or better.

## I.2.2 Current status

During LHC Run 1, the Higgs boson decay has been observed in the  $\gamma\gamma$ ,  $ZZ$ ,  $WW$  and  $\tau\tau$  channels. Considering one decay channel for a given production mode, production and decay rates are degenerate, and this is only the combination of channels which allows to extract particle couplings. The so-called  $\kappa$ -framework [7], based on coupling-strength modifiers, has been extensively in Run 1 to probe possible deviations with respect to predicted SM values. This is a tree level motivated framework, assuming only one single narrow resonance (zero-width approximation) and only modifications of coupling strengths are allowed (the tensor structure of the SM is preserved). From this basis, several models can be considered, doing further assumptions. For example, assuming the SM total width (i.e. no BSM decay allowed) the cross section  $\sigma(gg \rightarrow H \rightarrow \gamma\gamma)$  can be parameterized as:

$$\sigma(gg \rightarrow H \rightarrow \gamma\gamma) = \sigma_{SM}(gg \rightarrow H) \cdot \text{BR}_{SM}(H \rightarrow \gamma\gamma) \cdot \kappa_g^2 \cdot \kappa_\gamma^2,$$

where  $\kappa_g$  and  $\kappa_\gamma$  are respectively the (effective) gluon and photon coupling modifiers. Depending on the model, the effective couplings can be resolved in terms of the fundamental modifiers. The Figure 6 (a) shows the ATLAS-CMS Run 1 combined result for one resolved model (with six free coupling modifiers  $\kappa_W$ ,  $\kappa_Z$ ,  $\kappa_t$ ,  $\kappa_\tau$ ,  $\kappa_b$  and  $\kappa_\mu$ ). The uncertainties are 10% for  $\kappa_W$  and  $\kappa_Z$ , 16% for  $\kappa_t$  (indirect constraint), 15% for  $\kappa_\tau$  and 25% for  $\kappa_b$  (no sensitivity yet to  $\kappa_\mu$ ). Recent ATLAS and CMS Run 2 results on the  $bb$  decay channel and  $ttH$  production mode (both experiments being now above the  $3\sigma$  sensitivity threshold in both cases [8], [9], [10], [11]) will improve the corresponding coupling measurement in future combinations.

One fundamental property of the Higgs interaction is its scaling with the particle mass. The Figure 6 (b) illustrates nicely this linear behaviour: the parameters are defined as  $\sqrt{\kappa_V} \cdot m_F/v$  for the weak vector bosons (quadratic  $\kappa$  dependence because their masses directly result from the electroweak symmetry breaking) and as  $\kappa_F \cdot m_F/v$  for the fermions (linear  $\kappa$  dependence because they acquire masses via Yukawa interactions), where  $v = 246$  GeV is the vacuum expectation value of the Higgs field.

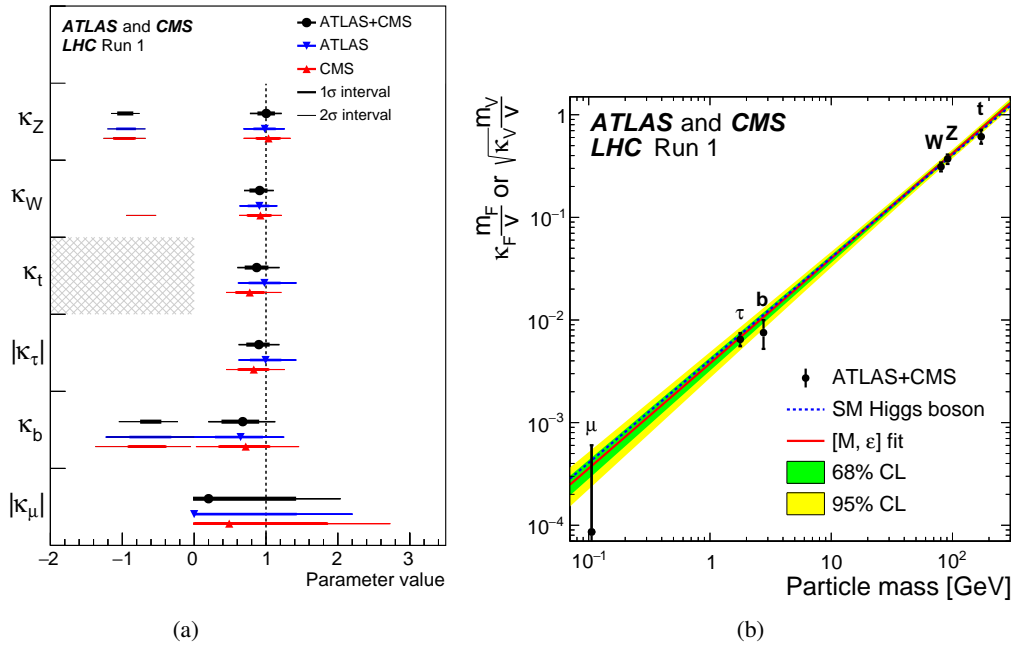


Figure 6: (a) Best fit values of the  $\kappa$ -parameters for the combination of ATLAS and CMS data [12]. (b) Best fit values as a function of particle mass for the combination of ATLAS and CMS data [12]. The parameters are defined as  $\kappa_F \cdot m_F/v$  for the fermions, and as  $\sqrt{\kappa_V} \cdot m_F/v$  for the weak vector bosons.

## Part II

### Preparing data: the long road from detector to analysis

*This chapter describes the various steps required to have data ready for producing physics results, from the proton-proton collisions up to the laptop disk. First the experimental conditions are described. Then data processing aspects are presented. Finally the work needed to reconstruct, identify and measure the particles from the detector response is illustrated for the particular case of the electron and photon energy calibration.*

#### II.1 The ATLAS detector at LHC

##### II.1.1 Overview of the detector

The ATLAS detector [13] at the LHC covers nearly the entire solid angle around the collision point<sup>1</sup>. It consists of an inner tracking detector surrounded by a thin superconducting solenoid, electromagnetic and hadronic calorimeters, and a muon spectrometer incorporating three large superconducting toroidal magnets. The inner-detector system (ID) is immersed in a 2 T axial magnetic field and provides charged particle tracking in the range  $|\eta| < 2.5$ . The high-granularity silicon pixel detector covers the vertex region and typically provides four measurements per track, the first hit being normally in the innermost layer: the insertable B-layer [14] (IBL) was installed before the start of Run 2 and is located at a distance of 3.3 cm in radius from the beam axis. It is followed by the silicon microstrip tracker which usually provides four two-dimensional measurement points per track. These silicon detectors are complemented by the transition radiation tracker, which enables radially extended track reconstruction up to  $|\eta| = 2.0$ . The transition radiation tracker also provides electron identification information based on the fraction of hits (typically 30 in total) above a higher energy deposit threshold corresponding to transition radiation. The calorimeter system covers the pseudorapidity range  $|\eta| < 4.9$ . Within the region  $|\eta| < 3.2$ , electromagnetic (EM) calorimetry is provided by barrel and endcap high-granularity lead/liquid-argon (LAr) electromagnetic calorimeters, with an additional thin LAr presampler covering  $|\eta| < 1.8$ , to correct for energy loss in material upstream of the calorimeters. Hadronic calorimetry is provided by the steel/scintillating-tile calorimeter, segmented into three barrel structures within  $|\eta| < 1.7$ , and two copper/LAr hadronic endcap calorimeters. The solid angle coverage is completed with forward copper/LAr and tungsten/LAr calorimeter modules optimised for electromagnetic and hadronic measurements respectively. The muon spectrometer (MS) comprises separate trigger and high-precision tracking chambers measuring the deflection of muons in a magnetic field generated by superconducting air-core toroids. The field integral of the toroids ranges between 2.0 and 6.0 T m across most of the detector. A set of precision chambers covers the region  $|\eta| < 2.7$  with three layers of monitored drift tubes, complemented by cathode strip chambers in the forward region, where the background is highest. The muon trigger system covers the range  $|\eta| < 2.4$  with resistive plate

---

<sup>1</sup> ATLAS uses a right-handed coordinate system with its origin at the nominal interaction point (IP) in the centre of the detector and the  $z$ -axis along the beam pipe. The  $x$ -axis points from the IP to the centre of the LHC ring, and the  $y$ -axis points upwards. Cylindrical coordinates  $(r, \phi)$  are used in the transverse plane,  $\phi$  being the azimuthal angle around the  $z$ -axis. The pseudorapidity is defined in terms of the polar angle  $\theta$  as  $\eta = -\ln \tan(\theta/2)$ . Angular distance is measured in units of  $\Delta R \equiv \sqrt{(\Delta\eta)^2 + (\Delta\phi)^2}$ .

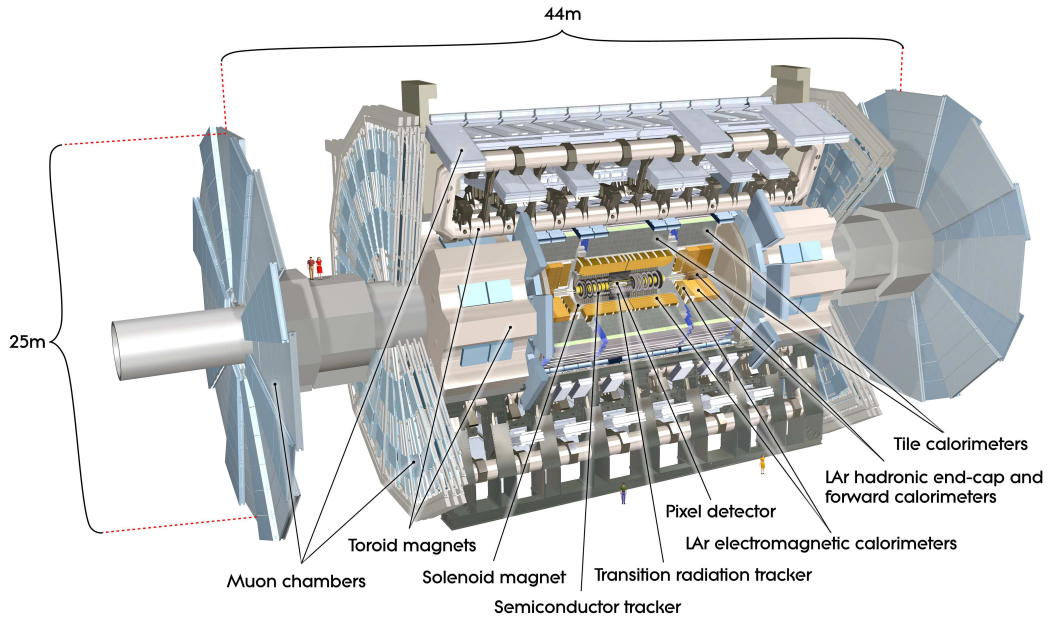


Figure 7: Overall view of the detector

chambers in the barrel, and thin gap chambers in the endcap regions. A two-level trigger system is used to select interesting events [15] at Run 2 (a three-level system was used at Run 1). The Level-1 trigger is implemented in hardware and uses a subset of detector information to reduce the event rate to a design value of at most 100 kHz. This is followed by a software-based high level trigger which reduces the event rate to about 1 kHz.

### II.1.2 LHC Run 2 conditions in 2015 and 2016

The LHC Run 2 covers the period 2015-2018; Figure 8 (a) shows the integrated luminosity (of proton-proton collisions) per year for ATLAS, up to 2017. The challenges at LHC Run 2 are the increases, with respect to LHC Run 1 conditions, of the centre-of-mass energy (from 8 TeV to 13 TeV) and of the instantaneous luminosity: in 2016, the instantaneous luminosity reached a maximum value of  $1.4 \cdot 10^{34} \text{ cm}^{-2}\text{s}^{-1}$ , corresponding to an increase by more than a factor two<sup>2</sup>. The consequence is a higher number of proton-proton interactions per bunch crossing, referred as (in-time) pileup events. The pileup profile for the analysed data is shown in Figure 8 (b): the mean value is 24. To be used for analysis, recorded data must satisfy data quality requirements, reflecting the good operational conditions of the various subdetectors. The corresponding global efficiency is above 90%. After such requirements, the dataset used for the results presented in this report amounts to an integrated luminosity of  $36.1 \text{ fb}^{-1}$  ( $3.2 \text{ fb}^{-1}$  in 2015 and  $32.9 \text{ fb}^{-1}$  in 2016).

<sup>2</sup> In 2017, the instantaneous luminosity reached the record value of  $2.1 \cdot 10^{34} \text{ cm}^{-2}\text{s}^{-1}$ , twice the design value.

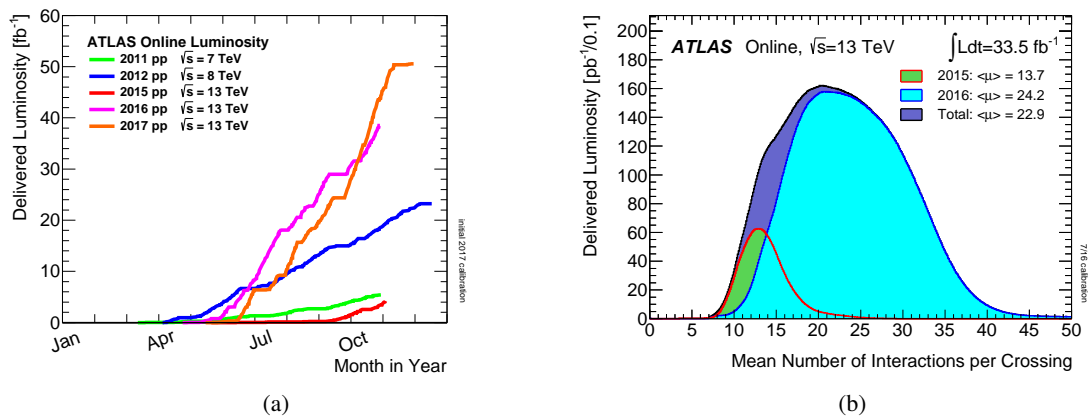


Figure 8: (a) LHC delivered luminosity to ATLAS versus time for the 2011-2017 period (pp collision data only). (b) Mean number of interactions per crossing for the 2015 and 2016 pp collision data.

## II.2 Data reconstruction, simulation and processing

### II.2.1 ATLAS data workflow

#### II.2.1.1 Data reconstruction

The prompt data correspond to all events selected at a total trigger rate of 1 kHz and written to the offline storage at the ATLAS Tier-0 facility at CERN. They are written in a RAW format, which merges the byte stream data written by the various subdetectors. They are reconstructed at the Tier-0: in this step, all the reconstruction algorithms are applied (tracking, energy calibration, etc.) and the data are converted from RAW to the primary physics analysis format, the Analysis Object Data (AOD). Both formats are then distributed to the ATLAS grid storage system for further processing. Before launching the main production, a prompt calibration loop is completed within 48 h, allowing to provide the most up-to-date conditions for the reconstruction (e.g. beam spot misalignment corrections).

#### II.2.1.2 Monte Carlo simulation

The Monte Carlo simulation workflow is more complex; it is shown in Figure 15. Inputs corresponding to generated hard process events (stored in EVNT files) are passed through the detector simulation

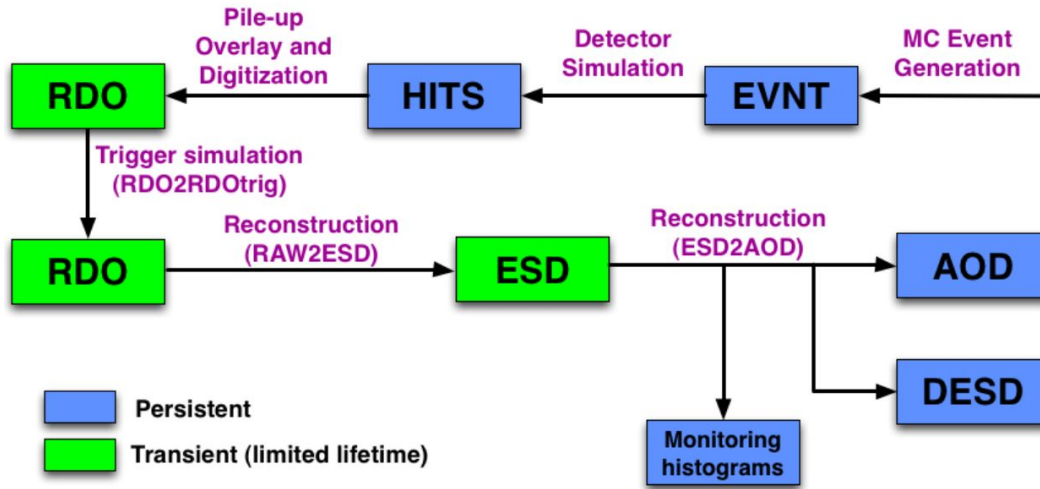


Figure 9: ATLAS Monte Carlo simulation data flow [17]

performed by GEANT4 [16], producing G4 hits files. The next step consists of the digitization, producing RDO files: the pileup (from simulated minimum bias events) is added in this step (digitization runs over merged hits). An extra RDO to RDO step is then required to add the trigger simulation (the key element here is to emulate the L1 hardware). From this point, the reconstruction steps are identical to the data ones.

## II.2.2 Shaping data for analysis

### II.2.2.1 The Run 2 analysis model

In Run 1, several practical difficulties were met by the collaboration in the data analysis. The main ones were a very inefficient usage of computing and disk resources and very long delays in the availability of the secondary (i.e. ‘ready-to-be-analysed’) data. To overcome these issues, a new analysis model has been designed, developed and commissioned during the LHC long shutdown 1 (2013-2014). This new model is illustrated in Figure 10. There are two key elements in this new model:

- the root-readability of the primary xAOD. This avoids the Run 1 issue to have many groups replicating in very large root files the content of the xAOD. This required large developments on the Event Data Model side.
- the derivation framework (also known as reduction framework): this is developed in the next section.

### II.2.2.2 The derivation framework

The derivation framework takes as input primary data coming from ATLAS reconstruction (the typical size of a dataset is a Petabyte) and produces secondary data (the typical size here is a Terabyte) targeting specific analyses (covering both performance and physics). About 100 different formats are used. This framework uses all the fundamental features of the ATLAS software, but its complexity is hidden

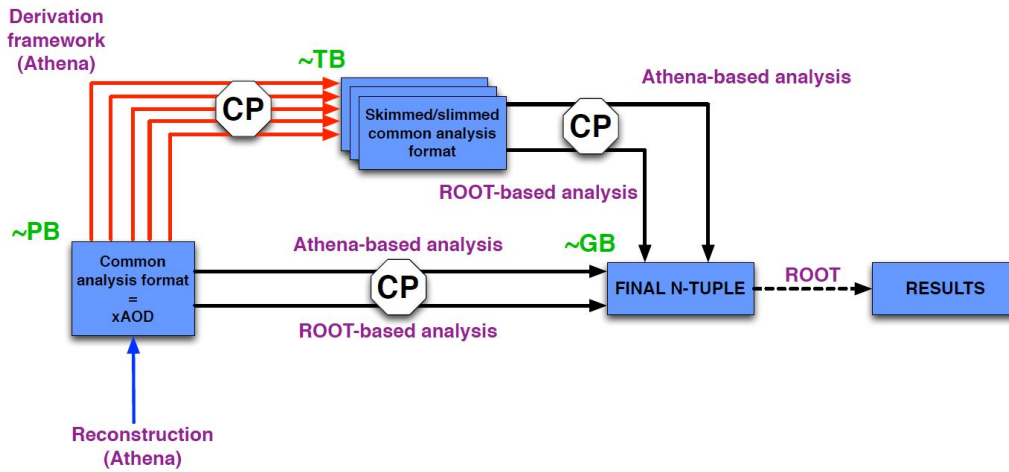


Figure 10: The Run 2 ATLAS data analysis model

behind an interface which allows users to configure quickly their format in python. Complex analysis tasks are executed via dedicated tools written in C++. In order to optimize the disk space required by the full set of derivations, several central tools have been developed to select events (skimming), objects (slimming) and variables (thinning): these various operations can be seen in the actual implementation in Athena sketched in Figure 11. The efficiency of such tools and their wide usage is critical to satisfy the global requirement that a full set of derivations does not occupy more disk space than the original xAOD. The size of the derivations (results produced from a Run 1 reprocessing campaign)<sup>3</sup> and the event overlap between derivations (pair-wise) are shown in Figure 12. In the case of derivations having a large overlap of events, the contents are required to be largely different (otherwise they are merged). In order to lighten the need in CPU and to decrease the turn-around time between data being reconstructed and ready for analysers, the production is made in train: from a single input multiple outputs are produced (multiple kernels in a single job are used). The xAOD access time is largely reduced by this technique and identical tasks are shared and executed only once (the output is first written in a common transient data store).

This framework has been used successfully since the start of the LHC Run 2 period in 2015. While adjustments are continuously needed to stay inside the CPU and disk boundaries (becoming more stringent with the steady increase of the collected datasets), no major change in the strategy is envisioned for Run 3.

### II.2.3 Contributions

- Data Reduction Task Force

I was co-coordinator (with James Catmore and Nurcan Ozturk) of this task force dedicated to the the development of the derivation framework (design phase in 2014). I worked in particular on the size reduction aspects and developed the so-called smart slimming technique: this technique allowed to reduce by a factor 3 the output size by selecting in an optimal way the variables needed for a given format.

<sup>3</sup> The trigger stream approach used at Run 1 has been changed for an inclusive stream approach.

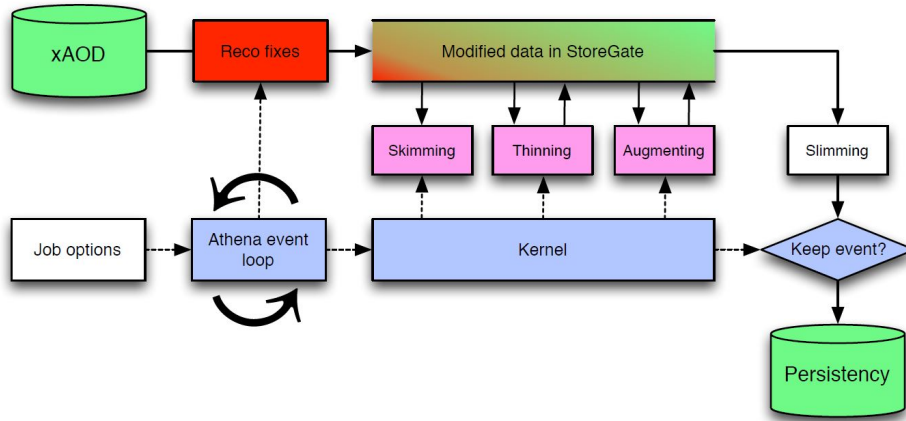


Figure 11: Implementation in Athena of the derivation framework [18]

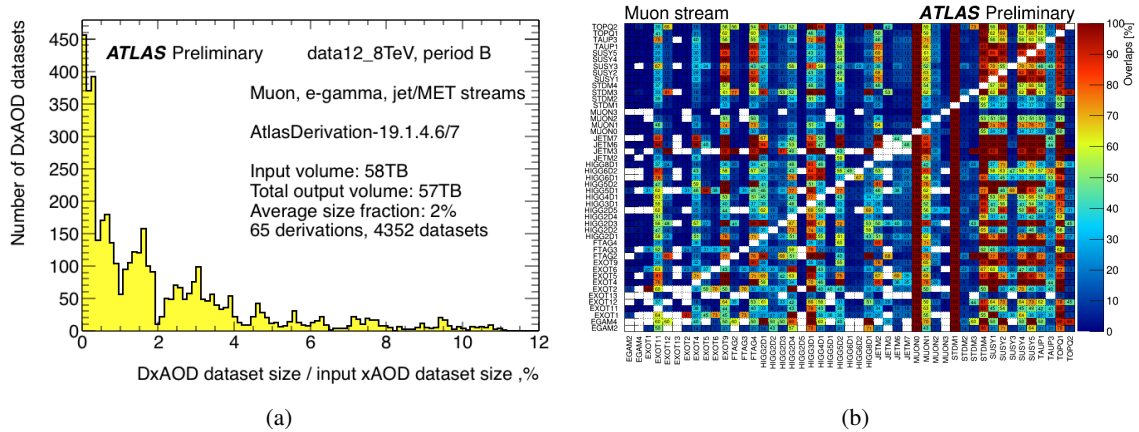


Figure 12: (a) Size of DxAO (derivation) datasets as a fraction of the size of the parent xAO datasets. (b) Event-wise fractional overlaps between derivations.

- Derivation software coordinator (2015)

I was responsible of all central software aspects and coordinating the work of about 40 people, each physics or combined performance group having one or two persons responsible of their software domain. This role was at the interface between the diverse activities of ATLAS (data preparation, reconstruction software, physics) and a key aspect was to planify in an optimal way the data and simulation production campaigns in the intense starting phase of Run 2.

## II.3 Electron and photon energy calibration

The understanding and control of the reconstruction and performance of the physics objects in the detector are crucial for all analyses. This represents tremendous efforts by the collaboration, as the set of objects and properties to measure is huge and requires to develop many sophisticated techniques (we can mention randomly the identification of displaced vertices in dense track environments, the

reconstruction efficiency of electrons, the flavour tagging of boosted jets or the momentum measurement of high energy muons). In this chapter, the particular case of the precision energy calibration of electrons and photons in the central part of the detector is presented.

### II.3.1 Overview of the calibration procedure

The energy reconstruction for EM objects is performed at two different levels: i) at cell (i.e. one readout LAr channel of a given depth sampling) level and ii) at cluster (i.e. a group of cells) level. The focus of this chapter is the cluster cell calibration, but for completeness, the description of the cell level reconstruction is first described in the next section.

#### II.3.1.1 LAr cell level reconstruction

The high precision part (up to  $\eta = 2.5$ ) of the LAr system is an EM calorimeter with a lead absorber (accordion geometry) and LAr acting as active material in the gap between absorber layers. The thickness is about 23 radiation lengths. The lateral and longitudinal granularity is sketched in Figure 13 (a); the  $\Delta\eta \times \Delta\Phi$  granularity in the barrel part is given in Table 1. Electrons and photons develop EM showers through their interaction with the absorber; these showers ionise the LAr inducing a current (proportional to the deposited energy) on copper readout electrodes. The  $\Phi$  granularity is obtained via dedicated summing boards (grouping 4 or 16 cells in  $\Phi$ ). Cables drive the signal up to front-end boards located just outside of the cryostat. The steps of the signal treatment applied on these boards can be seen in Figure 14: pre-amplification, amplification for three different gains (called low, medium and high) and shaping by a bipolar filter, sampling at the LHC clock frequency (40 MHz) and storing in switched capacitor arrays. Upon reception of a L1 trigger accept decision, four samples are transmitted via optical fibres to the backend system (located in a counting room next to the main ATLAS cavern) for further processing. The signal shaping and sampling are illustrated in Figure 13 (b). More details on the electronics chain can be found in Reference [19].

The energy reconstructed in a given cell at a given LHC bunch crossing is given by the following formula:

$$E_{\text{cell}} = F_{\mu\text{A} \rightarrow \text{MeV}} \times F_{\text{DAC} \rightarrow \mu\text{A}} \times \frac{1}{\frac{M_{\text{phys}}}{M_{\text{cali}}}} \times G \times \sum_{j=1}^{N_{\text{samples}}} a_j (s_j - p),$$

where:

- $s_j$  are the four signal samples measured in analog-to-digital converter counts
- $p$  is the readout electronics pedestal (measured in dedicated calibration runs)
- $a_j$  are the optimal filtering coefficients [20]
- $G$  is the gain factor measured for calibration pulses
- $\frac{M_{\text{phys}}}{M_{\text{cali}}}$  is the ratio of the maxima of physics to calibration pulse for the same input current
- $F_{\text{DAC} \rightarrow \mu\text{A}}$  is a calibration board conversion factor

- $F_{\mu A \rightarrow \text{MeV}}$  is the conversion factor from the measured current on the electrode to the deposited energy at the EM scale (determined from test beam studies).

### II.3.1.2 Cluster level calibration

The EM shower of an electron or a photon is much broader than the typical size of a calorimeter cell, which requires to reconstruct them in a cluster of cells. The first reconstruction step is based on a sliding-window technique through a  $\Delta\eta \times \Delta\phi = 0.025 \times 0.025$  grid, looking for cluster seeds above 2.5 GeV in transverse energy (the layers are summed longitudinally here). In addition to the calorimeter information, the tracker information is used to separate electrons, unconverted photons and converted photons (classified further in single-track and double-track conversions). Electron and photon clusters are built using windows of size  $3 \times 7$  (in units of layer 2 cells in  $\Delta\eta \times \Delta\phi$ ) and  $5 \times 5$ , in the barrel and in the endcap respectively). The lateral sizes have been optimized taking into account the global shower width and minimizing the impact of the noise. The complex chain of the following steps required to calibrate the energy response of electrons and photons is sketched in Figure 15:

- Step 1: Using EM cluster properties and information from the tracking system for converted photons, the energy is calibrated using a multivariate algorithm (MVA) trained on simulation, with the target set to the true energy of the particle (actually divided by the deposited accordion energy for performance reasons). The optimization is performed separately for electrons, converted and unconverted photons.
- Step 2: The energy scales of all layers are equalized between data and MC (the absolute scale adjustment (see Step 5) is not sufficient to have a correct extrapolation of the energy response over the full  $p_T$  range).
- Step 3: The MC-based MVA is applied to electrons and photons, similarly in data and simulation.
- Step 4: Some detector non-uniformities not simulated are corrected in data (e.g. the inter-module widening effect in the barrel).
- Step 5: The absolute energy scale in data is adjusted to simulation using  $Z \rightarrow ee$  events (template-based method). The energy resolution in data is found to be slightly larger than the simulation one: a smearing factor is extracted, and further applied to simulation. The correction factors are defined in fine  $\eta$  bins and applied in a similar way to electrons and photons.
- Step 6: The procedure is validated at low  $p_T$  for electrons using  $J/\Psi \rightarrow ee$  decays and for photons using  $Z \rightarrow ll\gamma$  events.

This strategy has been developed at Run 1. However many changes (new reconstruction release with a reduced number of samples, much higher pileup, insertion of the IBL leading to a large increase of material (services) in front of the endcaps, etc.) required to update all aspects for Run 2. The two aspects with the largest impact on the final photon energy uncertainty are discussed in the two next sections.



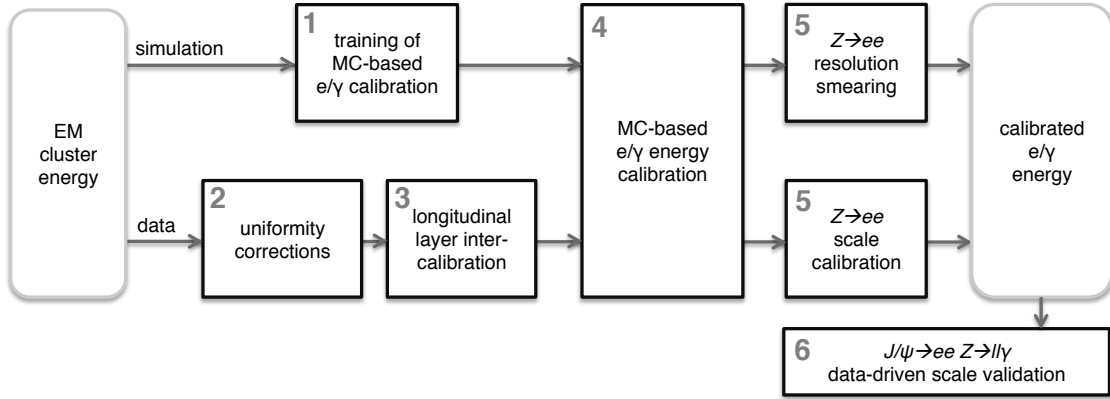


Figure 15: Schematic overview of the procedure used to calibrate the energy response of electrons and photons in ATLAS [21].

## II.3.2 Calorimeter layer intercalibration

### II.3.2.1 Overview of the method

The layer intercalibration is required to absorb effects not taken into account in the cell level electronics calibration. Most of the EM shower energy is deposited in the first two layers of the calorimeter, making their calibration crucial for a precise energy measurement: this is the topic discussed in this section. The presampler energy scale also needs to be adjusted: this calibration is performed using electrons from  $Z$  decay and unconverted photons with a small energy deposit in the presampler. The extraction of the presampler scale is made weakly sensitive to possible mismodellings of the passive material ahead of the presampler (inner detector, services and cryostat) by exploiting the correlation between the presampler energy and the energy ratio between the first and second layers (see Reference [22] for details). At the end, the presampler scale corrections obtained at Run 1 are very consistent with Run 2 values. The third layer of the EM calorimeter contributes to a very small fraction of the total deposited energy up to very high energy values (TeV scale): given its impact, no dedicated calibration is carried out.

For the intercalibration of the first two layers, muons from  $Z$  decays are used; the key advantage is that muons are insensitive to the amount of passive material ahead of the calorimeter. But the challenge is that they act as minimum-ionizing particles (MIP) leading to very small energy deposits, typically 60 MeV in layer 1 (L1) and 220 MeV in layer 2 (L2), i.e. two orders of magnitude smaller than the energy of selected electrons and photons). The typical energy distributions of the selected muons are shown in Figure 16. The cells crossed by the muon are determined by the extrapolation of the track to the calorimeter: three adjacent cells along  $\eta$  in L1 are used, and two adjacent cells along  $\Phi$  in L2 are used (the highest energy neighbour is chosen). This selection has been optimized from cross-talk modelling and pileup considerations: more cells reduce the impact of the cross-talk mismodelling but render the measurement more sensitive to pileup.

In order to extract the genuine muon calorimeter response, the observed muon energy distributions can be fitted by a Landau distribution (for the MIP) convoluted with a Gaussian distribution (for

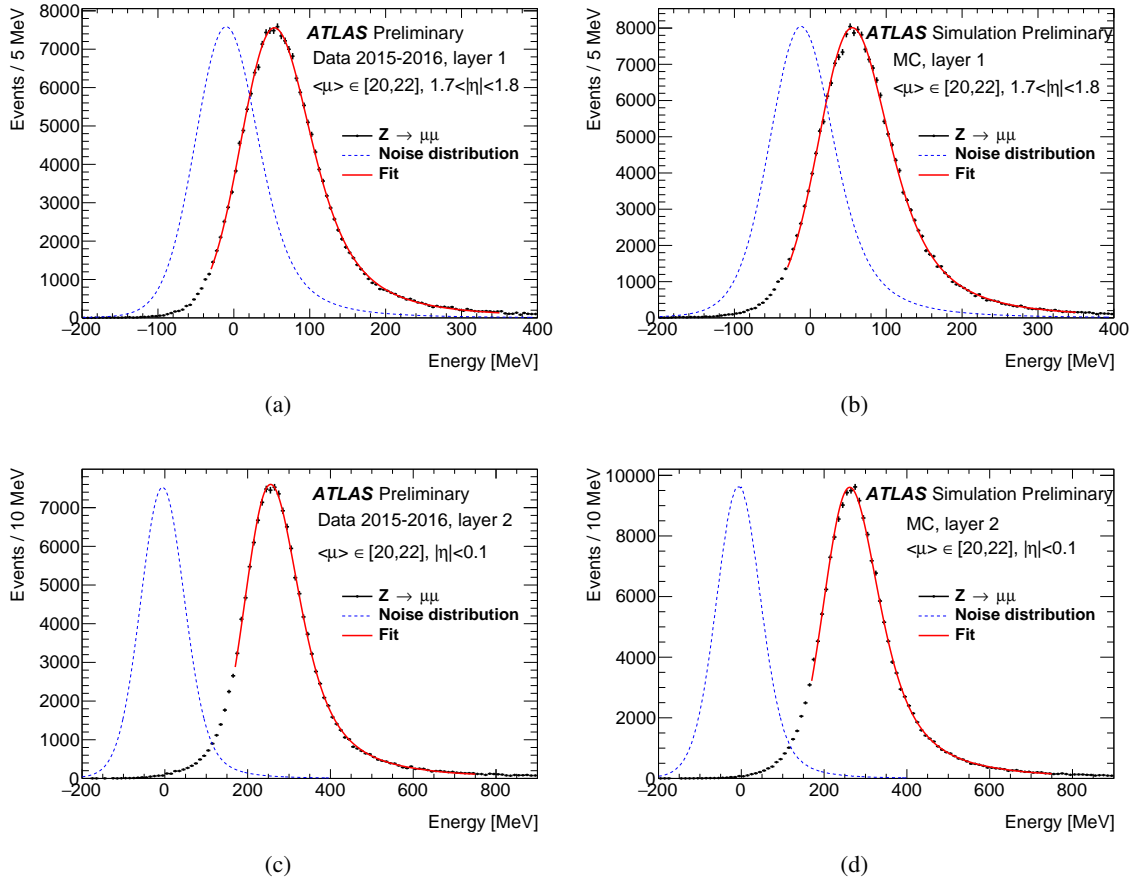


Figure 16: Distribution for one endcap bin of the energy loss by a muon in the first sampling of the EM calorimeter for data (a) and MC (b), and for one barrel bin in the the second sampling of the EM calorimeter for data (c) and MC (d). The results of fits performed with a Landau convoluted to a noise template are overlaid.

the electronics noise), or estimated by a truncated mean (TM) approach<sup>4</sup> (see Figures 16 and 17 respectively). From the extracted values (in bins of  $\eta$ ), the intercalibration result is defined as the double energy ratio  $\alpha_{1/2} = \langle E_{1/2} \rangle^{\text{data}} / \langle E_{1/2} \rangle^{\text{MC}}$ .

### II.3.2.2 Pileup dependency

Following discrepancies with respect to Run 1 for the intercalibration results, the pileup dependency was carefully investigated. The 2016 dataset was split in three low, medium and high regions of mean number of interactions per bunch crossing: very large discrepancies (up to 10% in the endcap) were observed. This showed the necessity to develop pileup mitigation techniques to be able to extract layer intercalibration corrections with muons in Run 2.

<sup>4</sup> All the plots presenting results based on the TM method have been kindly provided by O. Kivernyk.

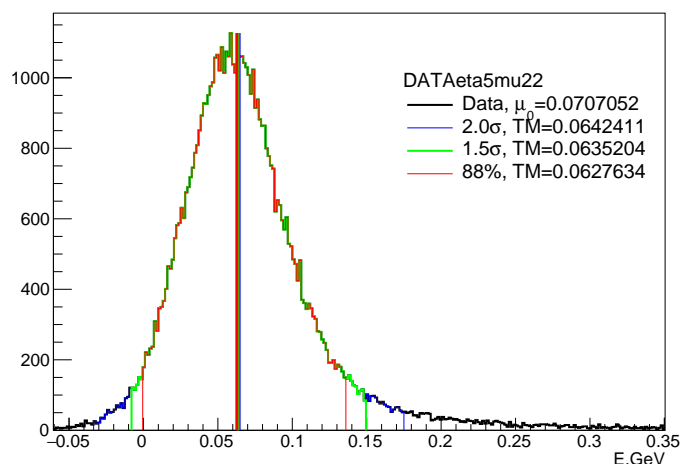


Figure 17: Truncated mean values computed for various range definitions: iterative procedure corresponding to intervals  $\mu_0 \pm 2 \cdot RMS$  (nominal case) and  $\mu_0 \pm 1.5 \cdot RMS$  where  $\mu_0$  is mean within initial range, and within smallest interval containing 88% of distribution.

### II.3.2.3 Pileup mitigation techniques

Various techniques were investigated, as applying isolation cuts, subtracting the average noise from neighbouring cells or removing the first part of the LHC bunch train<sup>5</sup> (biased from the absence of pileup compensation because of empty bunches before the start of the train). While some of them proved to reduce the pileup dependency, the remaining effects were still significant. The only successful technique found is the extrapolation in fine  $\mu$  slices towards  $\mu = 0$  (no pileup case). In this section, extrapolation results are presented for the TM method.

The used procedure consists of the following steps (repeated for all  $\eta$  bins):

- Extract the TM values for L1 and L2, in fine  $\mu$  slices, separately for data and MC.
- Fit the TM dependency versus  $\mu$  (linear fit) up to  $\mu = 0$ . The extrapolated value at  $\mu = 0$  provides the ‘true’ muon energy deposit, i.e. unbiased by pileup effects. The first data point corresponds to  $\mu \sim 12$ , while the MC sample used has a flat pileup profile from  $\mu = 1$  (see Figure 18).
- Compute the intercalibration results from the extrapolated values (see Figure 19).

A closure test of the method is performed on simulation by comparing the MC extrapolated results to the values of a MC sample generated without any pileup activity (pink curve on Figure 19). The agreement is better than 0.5% and 1% respectively in the barrel and the endcap, which validates the extrapolation approach.

<sup>5</sup> Most of the data were taken in the  $4 \times 72$  LHC filling scheme, which corresponds to trains of 288 proton bunches separated by a long gap.

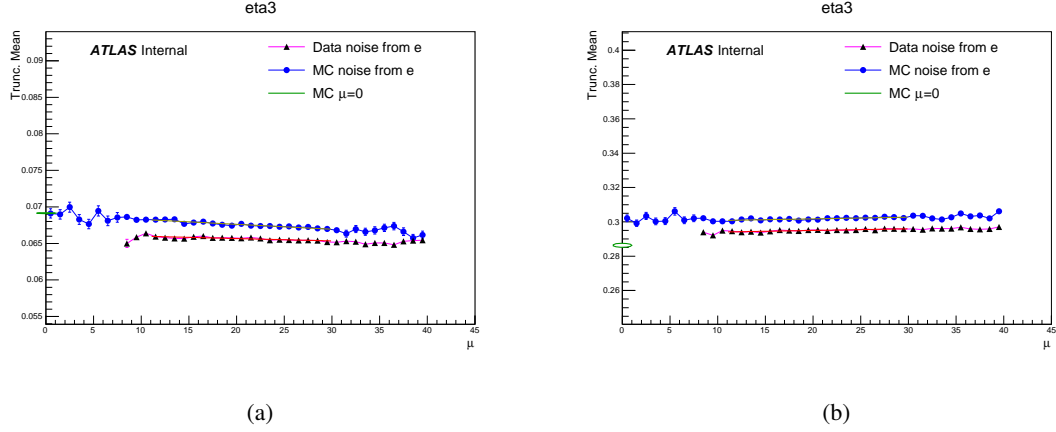


Figure 18: Truncated mean values as function of  $\mu$ , extracted from data and MC energy distributions of L1 (a) and L2 (b) for one barrel bin. TM values computed from the corresponding MC sample generated without pileup are also indicated.

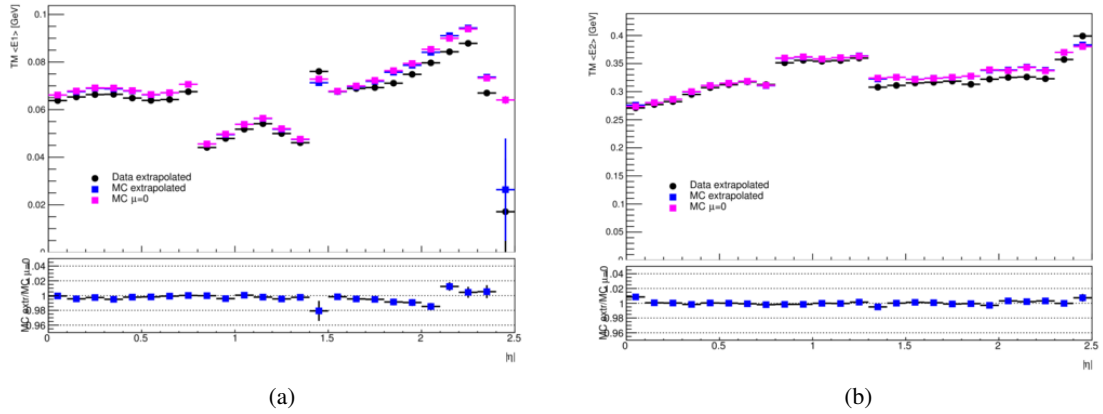


Figure 19: Truncated mean values computed as a function of  $|\eta|$  extracted from data and MC after extrapolation to  $\mu = 0$ . The corresponding TM values computed with MC without pileup are also indicated for crosscheck. Ratio panel shows the ratio of extrapolated MC to MC at  $\mu = 0$ .

### II.3.2.4 Final results

The final results are shown in Figure 20: the Landau results, the TM results and the average of the two methods are displayed. The main uncertainty sources are: the statistical accuracy of the extrapolation, the method closure systematics for each method, the modelling of energy leakage outside the two L2 cells used for the measurement and the method measurement assessed from the observed Landau-TM difference. At the end, in spite of a high pileup in Run 2, the accuracy of the measurement with muons is typically 1% in the barrel and 2% in the endcap (similar to Run 1).

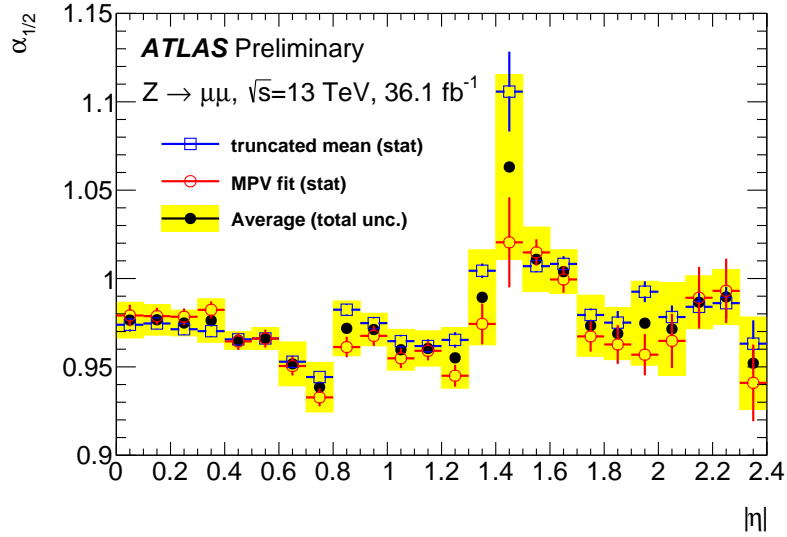


Figure 20: Comparison of the  $E_{1/2}^{\text{data}}/E_{1/2}^{\text{MC}}$  double ratio as a function of the corrected  $|\eta|$  coordinate for the 2015+2016 dataset. The blue points are the results for the TM method, the red points are the results for the Landau-based fit method and the black points show the average results.

### II.3.3 High to medium electronics gain non-linearity

#### II.3.3.1 Description of the effect and Run 1 observations

The global energy scale is adjusted in data to MC using electrons from Z decays (inclusively in energy), so non-linearity effects can induce uncertainties for the energy measurement of electrons and photons at higher or smaller energies. For each electronics amplification gain, the linearity is known to be better than 0.1% [19], but a relative miscalibration between gains (energy discontinuity in the energy region around the cell gain switch) can induce non-linearity effects. As most of the energy is deposited in L2, this is the only layer which matters for this effect and in the 1-100 GeV energy range, the relevant switch is the one from high to medium gain (cell threshold around 25 GeV in the barrel). In Run 1, this relative calibration was studied splitting the electrons from Z decays as a function of the recorded gain for the highest energy L2 cell: large discrepancies were found in some  $\eta$  regions (up to  $\sim 1\%$ ), as can be seen in Figure 21. The associated uncertainty proved to be the dominant systematic effect for the Run 1 Higgs boson mass measurement [4]. Further studies at the start of Run 2 [23] showed that i) using the latest MVA-based energy calibration, the effect is smaller (by a factor 2) and ii) the very large difference observed in the  $\eta$  region around 1.6 is mainly explained by lateral shower shape mismodellings. Given these findings, this gain miscalibration is studied with a new approach at Run 2.

#### II.3.3.2 2017 special run analysis

This relative miscalibration can be studied directly from data only under special conditions: the HG to MG transition threshold (for L2 cells) needs to be significantly lowered so that all the electrons from Z decays are recorded in MG. These data can then be compared to data taken under standard

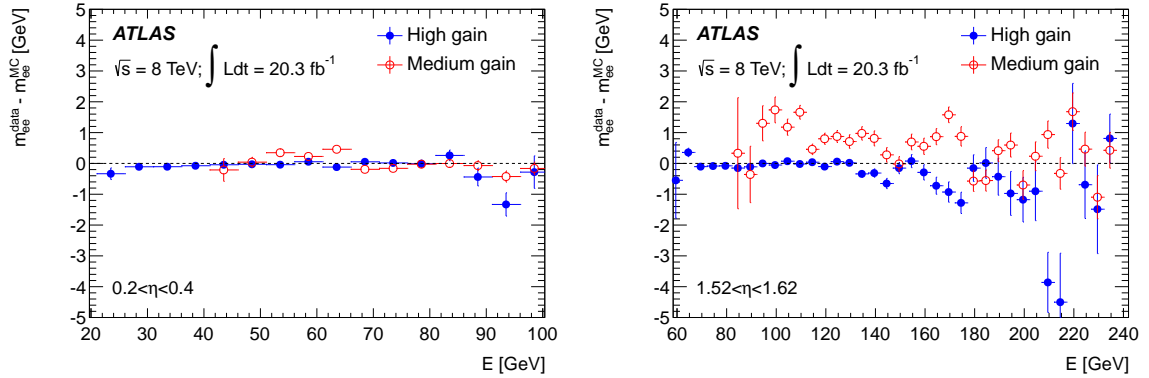


Figure 21: Difference between data and simulation of the average reconstructed  $Z$  boson mass as a function of the energy of one electron, for events where all cluster cells are in high gain from those where at least one cell is in medium gain, in a good region (top) and in a region with a significant bias (bottom) [22]. The error bars include statistical uncertainties only.

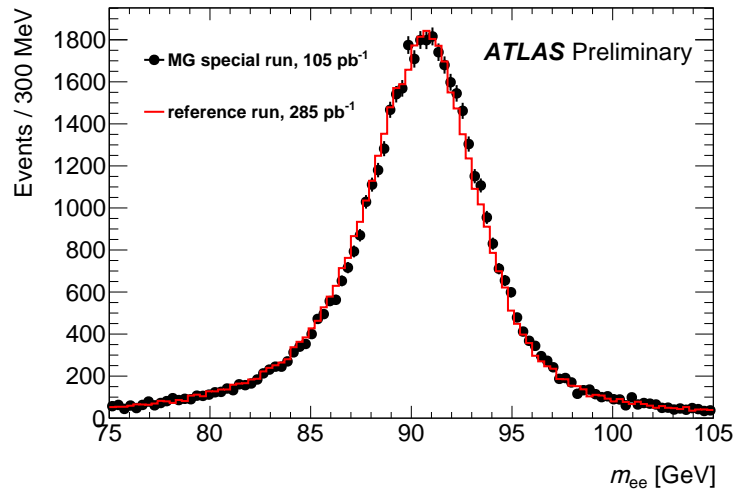


Figure 22: Distribution of the dielectron invariant mass for  $Z \rightarrow ee$  candidates recorded in 2017 during LHC fill 6035 (August 2nd, 2017). Data taken with a lower energy transition threshold between the high gain and medium gain for the L2 of the EM calorimeter are compared to data taken in the same LHC fill but with the standard thresholds.

conditions. An integrated luminosity of  $160 \text{ pb}^{-1}$  was recorded in these conditions in 2017; Figure 22 shows the special/standard comparison. The difference in the average value of the reconstructed mass is  $0.15 \pm 0.02\%$  (statistical uncertainty only), indicating a genuine (but small) relative miscalibration effect. Performing an extraction of  $\eta$ -dependent energy scale factors, the largest effect is observed in the  $\eta$  range 0.8-1.4 ( $\sim 0.5\%$ ). The final impact is then extrapolated from these factors over the full  $p_T$  range for electrons and photons using sensitivity factors (to this relative miscalibration) estimated on single particle simulated samples (in particular the fraction of HG/MG L2 cells as a function of  $p_T$  needs to be taken into account). For photons with  $p_T = 60 \text{ GeV}$ , the final uncertainty is between  $0.05\%$  and  $0.1\%$ , depending on  $\eta$ .

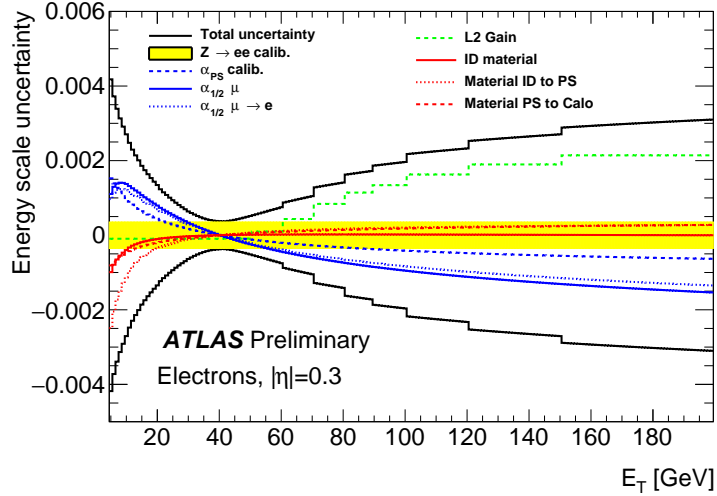


Figure 23: Energy scale calibration uncertainty for electrons as a function of  $p_T$  for  $|\eta| = 0.3$ . The total uncertainty is shown as well as the main contributions, which are represented with the signed impact of a one-sided variation of the corresponding systematic.

### II.3.4 Final systematic uncertainties and their correlations

In the previous sections, the two main sources of systematic uncertainty on the energy scale have been described in detail; their estimation was completely revisited for Run 2. But to take into account all effects affecting the extrapolation from  $Z$  decay electrons to photons or to electrons of different energies, 25 sources of uncertainty need actually to be considered. As several sources are considered as uncorrelated between  $\eta$  bins, the final set of nuisance parameters for the uncertainty model consists of 77 nuisance parameters. In Figure 23, the energy scale calibration uncertainty for electrons as a function of  $p_T$  is shown for one barrel bin. The main contributions are displayed: the relative L2 gain miscalibration, the layer intercalibration with muons and the associated extrapolation to electrons (due to simulation mismodellings which can bias the ‘true’ muon energy estimation), the  $Z \rightarrow ee$  in-situ scale and the material ahead of the accordion. For photons with  $p_T = 60$  GeV, the total calibration uncertainty is typically 0.4% in the barrel and 0.8% in the endcap.

All these results are currently being documented in a dedicated calibration paper and are used for an update of the Higgs boson mass measurement in the diphoton and 4-lepton channels with the 2015 + 2016 dataset.

### II.3.5 Contributions

- Electron and photon energy calibration group

I was co-convener (with Ruggero Turra and then Nansi Andari) of this group (for one year from October 2016). This group consists of about 30 people. I followed closely the work of about 10 students who have performed their qualification tasks (work needed to become an ATLAS author) on calibration during this period.

- Calibration software  
I was responsible of this software (tools to be used by the collaboration and specific calibration framework) for several years.
- Gain non-linearity  
I participated to the supervision of Kirill Grevtsov (PhD student at LAPP) on his work on this topic (see section [II.3.3](#)). His work led to a complete re-estimation of the associated systematics.
- Absolute energy scale determination  
I supervised, as PhD supervisor, the work of Saskia Falke (PhD student at LAPP) on this topic. She developed the so-called lineshape method, more flexible than the template method: results were used to assign a method systematics. R&D work is ongoing to extend this method to n-D energy scale factors.
- Calorimeter layer intercalibration  
I supervised the work of Oleh Kivernyk (postdoctorant at LAPP) on this topic (see section [II.3.2](#)). He produced results for the truncated mean approach.
- Editor of the supporting note on the systematics correlation model
- Co-editor of the being prepared Run 2 publication

## Part III

# Higgs boson coupling measurement in the diphoton channel with LHC Run 2 data

*This chapter describes the measurement of the different Higgs boson production mode cross sections via the diphoton decay channel. The main general aspects of the analysis are presented, but the emphasis is put on a new approach developed at Run 2, the so-called Simplified Template Cross Section measurement.*

All the results presented in this chapter come from Reference [24].

## III.1 The simplified template cross section framework

### III.1.1 Description of the framework

At Run 1, the Higgs boson coupling measurement focused on signal strengths and multiplicative coupling modifiers. But it is of primary importance to consider the possibilities to go beyond this approach, in order to maximize the physics output from such measurements and in particular to probe in an optimal way possible deviations from the SM predictions. One new framework conceptually combining coupling and differential cross section approaches, is based on Simplified Template Cross Sections (STXS); this approach is extensively described in Reference [6]. The main ideas are:

- to measure exclusive regions of phase space for specific production modes;
- to combine the measurements of all decay channels;
- to minimize the dependence on theory uncertainties, in order to ease the theory (re-)interpretation of the results;
- to isolate BSM sensitive regions;
- to retain the maximal experimental sensitivity (e.g. by using MVA techniques).

One key aspect of this approach is to decouple as much as possible theory uncertainties from the measurements. For instance, all measurements are restricted to the phase space region  $|y_H| < 2.5$ , where  $|y_H|$  is the Higgs boson rapidity, because there is no experimental sensitivity at all outside this range (detector coverage); such a restriction avoids the extrapolation to the full phase space and the associated uncertainty. The branching ratios are also folded into the measurements (no assumption on their values). With the increasing size of the datasets, a more and more fine granularity of the probed phase space regions (called truth bins in the following) will be accessible. A given granularity is referred as ‘stage’ in Reference [6]: the presented analysis is based on stage 1. Figure 24 shows the various truth bins considered for the ggF production mode (a) and the VBF production mode (b). The ggF categorization is based mainly on the jet multiplicity and the Higgs boson  $p_T$ . The VBF categorization introduces VBF topology cuts (required at reconstruction level to keep under control the ggF contamination); the VH (V hadronic) production is included in the VBF categorization (in a

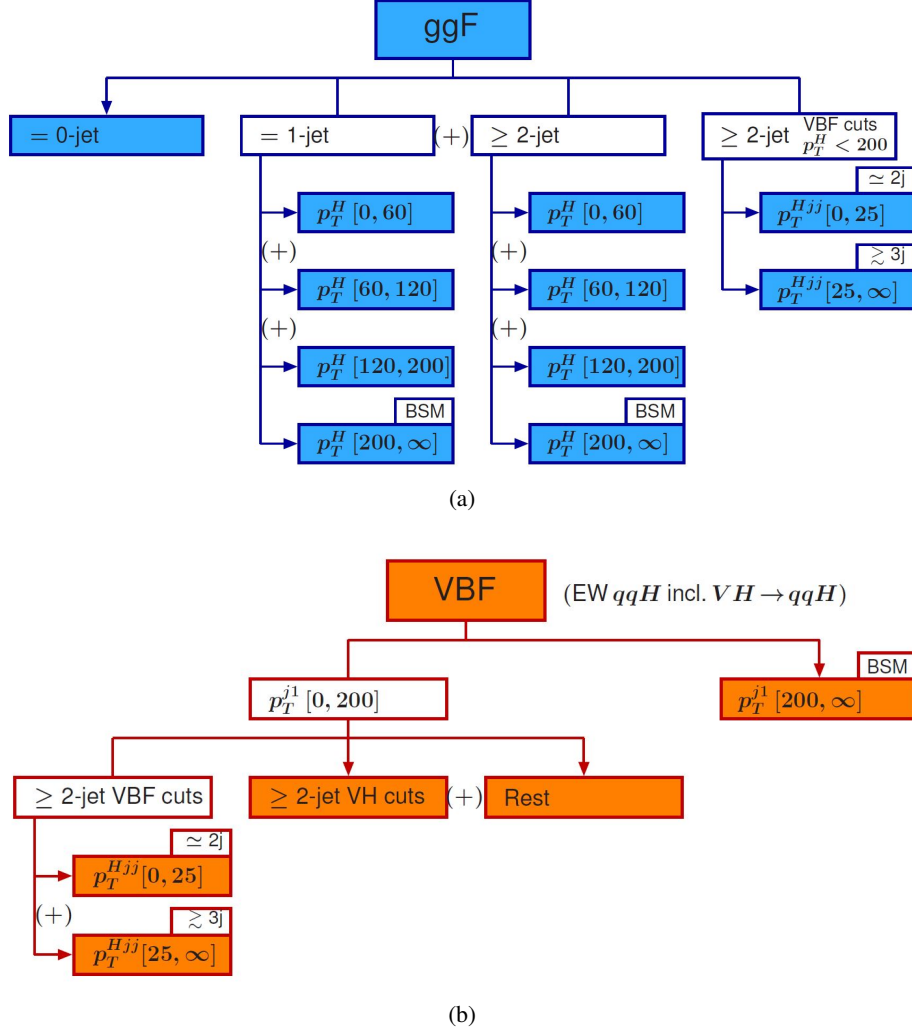


Figure 24: (a) Stage 1 binning for the gluon fusion production [6]. (b) Stage 1 binning for the vector fusion production [6].

dedicated truth bin). It is important to stress that truth level and reconstruction level categories need to be defined consistently to maximize the measurement sensitivity (there were a lot of discussions on this point).

### III.1.2 Merging scheme used in the analysis

Considering all production modes, the stage-1 splitting defines 31 truth bins (see the right column of Table 2.). Since the current dataset does not provide a sufficient statistical power for all truth bins, it is required to merge many bins: the guiding rule is to define bins with at minimum a  $1\sigma$  sensitivity to the SM rate. In particular, all the VH (V leptonic) truth bins are merged, as well as the top associated production mode truth bins. Six ggF truth bins and two VBF truth bins are used. This leads to a total of ten truth bins. One special case concerns the ‘BSM’ ggF and VBF truth bins (see Figure 24). They are strongly anti-correlated and the current analysis is not sensitive to their yield difference. For

Process	Measurement region	Particle-level stage-1 region
$ggH + gg \rightarrow Z(\rightarrow qq)H$	0-jet	0-jet
	1-jet, $p_T^H < 60$ GeV 1-jet, $60 \leq p_T^H < 120$ GeV 1-jet, $120 \leq p_T^H < 200$ GeV $\geq 1$ -jet, $p_T^H > 200$ GeV	1-jet, $p_T^H < 60$ GeV 1-jet, $60 \leq p_T^H < 120$ GeV 1-jet, $120 \leq p_T^H < 200$ GeV 1-jet, $p_T^H > 200$ GeV $\geq 2$ -jet, $p_T^H > 200$ GeV $\geq 2$ -jet, $p_T^H < 60$ GeV $\geq 2$ -jet, $60 \leq p_T^H < 120$ GeV $\geq 2$ -jet, $120 \leq p_T^H < 200$ GeV VBF-like, $p_T^{Hjj} < 25$ GeV VBF-like, $p_T^{Hjj} \geq 25$ GeV
$qq' \rightarrow Hqq'$ (VBF + $VH$ )	$p_T^j < 200$ GeV	$p_T^j < 200$ GeV, VBF-like, $p_T^{Hjj} < 25$ GeV $p_T^j < 200$ GeV, VBF-like, $p_T^{Hjj} \geq 25$ GeV $p_T^j < 200$ GeV, $VH$ -like $p_T^j < 200$ GeV, Rest
	$p_T^j > 200$ GeV	$p_T^j > 200$ GeV
$VH$ (leptonic decays)	$VH$ leptonic	$q\bar{q} \rightarrow ZH, p_T^Z < 150$ GeV
		$q\bar{q} \rightarrow ZH, 150 < p_T^Z < 250$ GeV, 0-jet
		$q\bar{q} \rightarrow ZH, 150 < p_T^Z < 250$ GeV, $\geq 1$ -jet
		$q\bar{q} \rightarrow ZH, p_T^Z > 250$ GeV
		$q\bar{q} \rightarrow WH, p_T^W < 150$ GeV
		$q\bar{q} \rightarrow WH, 150 < p_T^W < 250$ GeV, 0-jet
		$q\bar{q} \rightarrow WH, 150 < p_T^W < 250$ GeV, $\geq 1$ -jet
		$q\bar{q} \rightarrow WH, p_T^W > 250$ GeV
		$gg \rightarrow ZH, p_T^Z < 150$ GeV
		$gg \rightarrow ZH, p_T^Z > 150$ GeV, 0-jet
$gg \rightarrow ZH, p_T^Z > 150$ GeV, $\geq 1$ -jet		
Top-associated production	top	$t\bar{t}H$
		$W$ -associated $tH(tHW)$ $t$ -channel $tH(tHq\bar{b})$
$bbH$	merged w/ $ggH$	$bbH$

Table 2: Merging scheme used in the analysis, reducing the 31 phase space regions of the stage-1 model (right column) to 10 phase space regions (middle column) [24].

this reason, only the sum of these two bins is measured (the yield difference is included as a nuisance parameter), leading to nine measured cross sections.

## III.2 Overview of the analysis

### III.2.1 Event simulation

The signal samples use state-of-the-art MC generators and theory cross section predictions (up to N<sup>3</sup>LO for  $ggF$ , which corresponds to a computation with  $\sim 100.000$  Feynman diagrams). Table 3 summarizes the generators used for signal and background samples. For the irreducible diphoton

Table 3: Summary of the event generators and PDF sets used to model the signal and the main background processes. The SM cross sections  $\sigma$  for the Higgs production processes with  $m_H = 125.09$  GeV are also given separately for  $\sqrt{s} = 13$  TeV, together with the orders of the calculations corresponding to the quoted cross sections, which are used to normalize the samples, after multiplication by the Higgs boson branching ratio to diphotons, 0.227% [24].

Process	Generator	Showering	PDF set	$\sigma$ [pb] $\sqrt{s} = 13$ TeV	Order of calculation of $\sigma$
ggH	POWHEG NNLOPS	PYTHIA8	PDF4LHC15	48.52	N <sup>3</sup> LO(QCD)+NLO(EW)
VBF	POWHEG BOX	PYTHIA8	PDF4LHC15	3.78	NNLO(QCD)+NLO(EW)
WH	POWHEG BOX	PYTHIA8	PDF4LHC15	1.37	NNLO(QCD)+NLO(EW)
$q\bar{q}' \rightarrow ZH$	POWHEG BOX	PYTHIA8	PDF4LHC15	0.76	NNLO(QCD)+NLO(EW)
$gg \rightarrow ZH$	POWHEG BOX	PYTHIA8	PDF4LHC15	0.12	NLO+NLL(QCD)
$t\bar{t}H$	MADGRAPH5_AMC@NLO	PYTHIA8	NNPDF3.0	0.51	NLO(QCD)+NLO(EW)
$b\bar{b}H$	MADGRAPH5_AMC@NLO	PYTHIA8	CT10	0.49	5FS(NNLO)+4FS(NLO)
$t$ -channel $tH$	MADGRAPH5_AMC@NLO	PYTHIA8	CT10	0.07	4FS(LO)
$W$ -associated $tH$	MADGRAPH5_AMC@NLO	HERWIG++	CT10	0.02	5FS(NLO)
$\gamma\gamma$	SHERPA	SHERPA	CT10		LO
$V\gamma\gamma$	SHERPA	SHERPA	CT10		LO

background, a fast simulation is used because of the very high statistics required (this will be justified later); full simulation samples are used for all the rest.

### III.2.2 Event selection

The description of the reconstruction of photons and their energy calibration can be found in Section II.3.1.2. To reject the fake photon background (dominated by neutral hadrons decaying into photon pairs), identification criteria based on lateral and longitudinal shower shapes are applied. Two working points are defined, called *loose* and *tight*. Track-based and calorimeter isolation criteria are also used to further reduce the hadronic background contamination.

At trigger level, the event selection starts with a diphoton trigger signature requiring the presence of two *loose* photons with asymmetric  $E_T$  cuts, 35 GeV and 25 GeV respectively. Offline, the first selection step is the choice of the diphoton primary vertex: using the two highest  $p_T$  photon candidates (in the acceptance range  $|\eta| < 2.37$  excluding the transition region), a neural-network algorithm, combining primary vertex and pointing information (from the two photon directions, thanks to the longitudinal sampling of the calorimeter) selects the highest probability vertex. From simulation, the efficiency is estimated to be  $\sim 80\%$  for ggF events, and higher for other production modes (due to the presence of extra jets or leptons). The Figure 25 illustrates the behaviour of the efficiency of the neural-network algorithm versus the number of primary vertex candidates; the comparison between the Run 1 version (violet squares) and the Run 2 version (blue circles) shows that the re-tuned version has a much better pileup robustness. The final kinematic diphoton selection uses relative kinematic cuts,  $E_T/m_{\gamma\gamma} > 0.35$  and 0.25 respectively for the leading and subleading photons.

The reconstruction and selection of other objects (jets, b-jets, leptons and missing transverse energy) are based on standard ATLAS criteria [24]. The jet kinematic selection, relevant for the VBF-related measurements, is the following: jets are required to have  $p_T > 25$  GeV for  $|\eta| < 2.4$  and  $p_T > 30$  GeV for  $2.4 < |\eta| < 4.4$ .

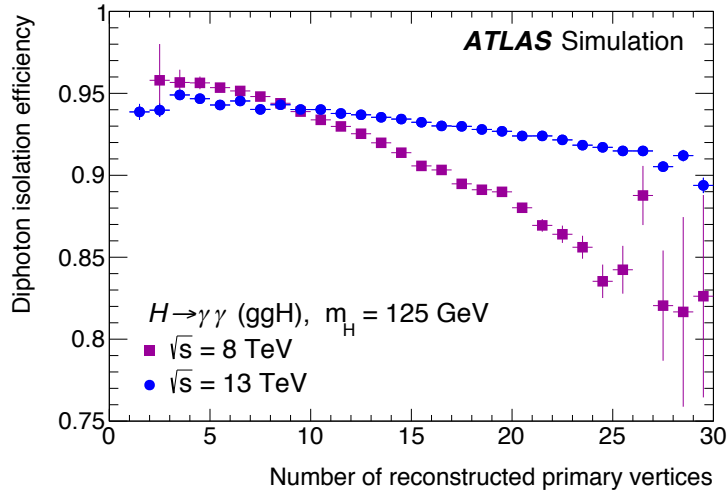


Figure 25: Efficiency for both photons to fulfill the isolation requirement as a function of the number of primary vertex candidates in each event (estimated on a simulation sample of ggF events) [24].

### III.2.3 Event categorization

The events selected are classified into 31 exclusive categories: these categories, defined from the event topology and kinematics, are optimized to maximize the sensitivity for the cross section measurement of the nine phase space regions defined from the merging of stage-1 truth bins. This requires i) to have reconstruction categories with kinematic thresholds close (or identical) to the ones used at truth level and ii) to have the largest purity of the targeted production mode inside a given reconstruction category. In order to obtain orthogonal categories, this categorization is applied in sequence, from the production mode with the smallest cross section to the highest one: ttH, VH, VBF and ggF. Table 4 summarizes the selection criteria defining all categories. Three boosted decision trees (BDT) are used to enhance the separation between production modes (in the ttH hadronic, VH hadronic and VBF categories). The numbers of expected signal and background events in all reconstruction categories are given in Table 5. The expected signal yield per category varies from 0.5 to  $\sim 600$  signal events. The truth bin purity per reconstruction bin is shown in Figure 26 for the complete stage-1 splitting. A good diagonal structure is observed (a purely diagonal structure is the ideal case) and this is due to the close correspondence between truth bins and reconstruction categories. The main outliers come from the ggF contamination in the VBF reconstruction categories (typically 30% before using multivariate techniques), which is the general challenge for the VBF-related measurements (not specific to the framework considered).

### III.2.4 Signal and background modelling

#### III.2.4.1 Signal modelling

Thanks to the excellent photon energy resolution of the LAr calorimeter, the Higgs signal appears as a narrow peak over the steeply falling background. The signal model is defined in each reconstruction

Category	Selection
tH lep 0fwd	$N_{\text{lep}} = 1, N_{\text{jets}}^{\text{cen}} \leq 3, N_{b\text{-tag}} \geq 1, N_{\text{jets}}^{\text{fwd}} = 0 (p_{\text{T}}^{\text{jet}} > 25 \text{ GeV})$
tH lep 1fwd	$N_{\text{lep}} = 1, N_{\text{jets}}^{\text{cen}} \leq 4, N_{b\text{-tag}} \geq 1, N_{\text{jets}}^{\text{fwd}} \geq 1 (p_{\text{T}}^{\text{jet}} > 25 \text{ GeV})$
ttH lep	$N_{\text{lep}} \geq 1, N_{\text{jets}}^{\text{cen}} \geq 2, N_{b\text{-tag}} \geq 1, Z\ell\ell \text{ veto } (p_{\text{T}}^{\text{jet}} > 25 \text{ GeV})$
ttH had BDT1	$N_{\text{lep}} = 0, N_{\text{jets}} \geq 3, N_{b\text{-tag}} \geq 1, \text{BDT}_{\text{ttH}} > 0.92$
ttH had BDT2	$N_{\text{lep}} = 0, N_{\text{jets}} \geq 3, N_{b\text{-tag}} \geq 1, 0.83 < \text{BDT}_{\text{ttH}} < 0.92$
ttH had BDT3	$N_{\text{lep}} = 0, N_{\text{jets}} \geq 3, N_{b\text{-tag}} \geq 1, 0.79 < \text{BDT}_{\text{ttH}} < 0.83$
ttH had BDT4	$N_{\text{lep}} = 0, N_{\text{jets}} \geq 3, N_{b\text{-tag}} \geq 1, 0.52 < \text{BDT}_{\text{ttH}} < 0.79$
tH had 4j1b	$N_{\text{lep}} = 0, N_{\text{jets}}^{\text{cen}} = 4, N_{b\text{-tag}} = 1 (p_{\text{T}}^{\text{jet}} > 25 \text{ GeV})$
tH had 4j2b	$N_{\text{lep}} = 0, N_{\text{jets}}^{\text{cen}} = 4, N_{b\text{-tag}} \geq 2 (p_{\text{T}}^{\text{jet}} > 25 \text{ GeV})$
VH dilep	$N_{\text{lep}} \geq 2, 70 \text{ GeV} \leq m_{\ell\ell} \leq 110 \text{ GeV}$
VH lep High	$N_{\text{lep}} = 1,  m_{e\gamma} - 89 \text{ GeV}  > 5 \text{ GeV}, p_{\text{T}}^{\ell+E_{\text{T}}^{\text{miss}}} > 150 \text{ GeV}$
VH lep Low	$N_{\text{lep}} = 1,  m_{e\gamma} - 89 \text{ GeV}  > 5 \text{ GeV}, p_{\text{T}}^{\ell+E_{\text{T}}^{\text{miss}}} < 150 \text{ GeV}, E_{\text{T}}^{\text{miss}} \text{ significance} > 1$
VH MET High	$150 \text{ GeV} < E_{\text{T}}^{\text{miss}} < 250 \text{ GeV}, E_{\text{T}}^{\text{miss}} \text{ significance} > 9 \text{ or } E_{\text{T}}^{\text{miss}} > 250 \text{ GeV}$
VH MET Low	$80 \text{ GeV} < E_{\text{T}}^{\text{miss}} < 150 \text{ GeV}, E_{\text{T}}^{\text{miss}} \text{ significance} > 8$
jet BSM	$p_{\text{T},j1} > 200 \text{ GeV}$
VH had tight	$60 \text{ GeV} < m_{ij} < 120 \text{ GeV}, \text{BDT}_{\text{VH}} > 0.78$
VH had loose	$60 \text{ GeV} < m_{ij} < 120 \text{ GeV}, 0.35 < \text{BDT}_{\text{VH}} < 0.78$
VBF tight, high $p_{\text{T}}^{\text{H}jj}$	$ \Delta\eta_{jj}  > 2,  \eta_{\gamma\gamma} - 0.5(\eta_{j1} + \eta_{j2})  < 5, p_{\text{T}}^{\text{H}jj} > 25 \text{ GeV}, \text{BDT}_{\text{VBF}} > 0.47$
VBF loose, high $p_{\text{T}}^{\text{H}jj}$	$ \Delta\eta_{jj}  > 2,  \eta_{\gamma\gamma} - 0.5(\eta_{j1} + \eta_{j2})  < 5, p_{\text{T}}^{\text{H}jj} > 25 \text{ GeV}, -0.32 < \text{BDT}_{\text{VBF}} < 0.47$
VBF tight, low $p_{\text{T}}^{\text{H}jj}$	$ \Delta\eta_{jj}  > 2,  \eta_{\gamma\gamma} - 0.5(\eta_{j1} + \eta_{j2})  < 5, p_{\text{T}}^{\text{H}jj} < 25 \text{ GeV}, \text{BDT}_{\text{VBF}} > 0.87$
VBF loose, low $p_{\text{T}}^{\text{H}jj}$	$ \Delta\eta_{jj}  > 2,  \eta_{\gamma\gamma} - 0.5(\eta_{j1} + \eta_{j2})  < 5, p_{\text{T}}^{\text{H}jj} < 25 \text{ GeV}, 0.26 < \text{BDT}_{\text{VBF}} < 0.87$
ggH 2J BSM	$\geq 2 \text{ jets}, p_{\text{T}}^{\gamma\gamma} \geq 200 \text{ GeV}$
ggH 2J High	$\geq 2 \text{ jets}, p_{\text{T}}^{\gamma\gamma} \in [120, 200] \text{ GeV}$
ggH 2J Med	$\geq 2 \text{ jets}, p_{\text{T}}^{\gamma\gamma} \in [60, 120] \text{ GeV}$
ggH 2J Low	$\geq 2 \text{ jets}, p_{\text{T}}^{\gamma\gamma} \in [0, 60] \text{ GeV}$
ggH 1J BSM	$= 1 \text{ jet}, p_{\text{T}}^{\gamma\gamma} \geq 200 \text{ GeV}$
ggH 1J High	$= 1 \text{ jet}, p_{\text{T}}^{\gamma\gamma} \in [120, 200] \text{ GeV}$
ggH 1J Med	$= 1 \text{ jet}, p_{\text{T}}^{\gamma\gamma} \in [60, 120] \text{ GeV}$
ggH 1J Low	$= 1 \text{ jet}, p_{\text{T}}^{\gamma\gamma} \in [0, 60] \text{ GeV}$
ggH 0J Fwd	$= 0 \text{ jets}, \text{one photon with }  \eta  > 0.95$
ggH 0J Cen	$= 0 \text{ jets}, \text{two photons with }  \eta  \leq 0.95$

Table 4: Event selection of the 31 reconstruction categories [24].

Category	$S_{90}$	$B_{90}$	$f_{90}$	$Z_{90}$
ttH lep 0fwd	0.93	3.6	0.21	0.47
ttH lep 1fwd	0.99	1.9	0.34	0.67
ttH lep	2.1	2.7	0.44	1.16
ttH had BDT1	1.3	2.0	0.40	0.85
ttH had BDT2	1.6	3.9	0.29	0.75
ttH had BDT3	0.54	2.3	0.19	0.35
ttH had BDT4	2.2	14.0	0.14	0.58
tH had 4j1b	2.3	48	0.05	0.32
tH had 4j2b	0.56	6.8	0.08	0.21
VH dilep	0.84	1.1	0.43	0.72
VH lep High	1.4	2.4	0.37	0.82
VH lep Low	5.8	52	0.10	0.79
VH MET High	1.2	2.3	0.34	0.72
VH MET Low	0.56	3.4	0.14	0.30
jet BSM	24	280	0.08	1.41
VH had tight	11	47	0.19	1.55
VH had loose	15	220	0.06	0.98
VBF tight, high $p_T^{Hjj}$	18	120	0.13	1.62
VBF loose, high $p_T^{Hjj}$	15	250	0.06	0.93
VBF tight, low $p_T^{Hjj}$	12	12	0.50	3.12
VBF loose, low $p_T^{Hjj}$	17	110	0.14	1.62
ggH 2J BSM	6.8	26	0.21	1.29
ggH 2J High	26	280	0.08	1.53
ggH 2J Med	65	1700	0.04	1.56
ggH 2J Low	73	3100	0.02	1.30
ggH 1J BSM	2.0	7.1	0.22	0.72
ggH 1J High	28	240	0.11	1.80
ggH 1J Med	140	2900	0.05	2.61
ggH 1J Low	260	8000	0.03	2.89
ggH 0J Fwd	520	21000	0.02	3.62
ggH 0J Cen	300	5300	0.05	4.07

Table 5: The numbers of background events  $B_{90}$ , measured by fits to the data, in the smallest interval expected to contain 90% of the SM signal events  $S_{90}$  (typically 3 GeV), accompanied by the expected purities  $f_{90} \equiv S_{90}/(S_{90} + B_{90})$  and expected significances  $Z_{90} \equiv \sqrt{2((S_{90} + B_{90}) \log(1 + S_{90}/B_{90}) - S_{90})}$  (adapted from Reference [24]).

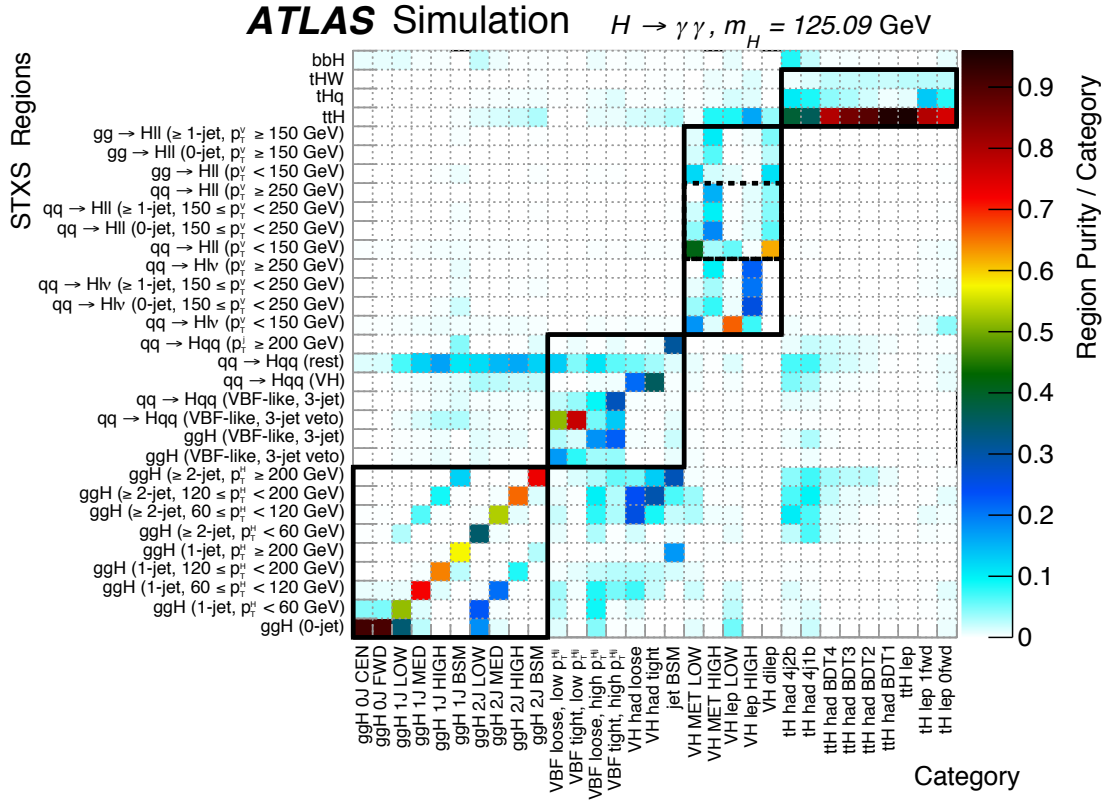


Figure 26: The fraction of signal events assigned to each reconstructed category ( $x$  axis) and originating from a given region of the stage-1 simplified template cross section framework ( $y$  axis). The black lines separate the  $t\bar{t}H$  and  $tH$ ,  $VH$  leptonic,  $VH$  hadronic and VBF enriched, and untagged categories, along with the simplified template cross-section regions they are most sensitive to. The color shows the purity of the region per category [24].

category from fits to simulated signal samples. In all categories, an empirical double-sided Crystal Ball function is used; the Figure 27 shows the parametrizations for two different categories with (significantly) different mass resolutions, 1.6 GeV and 2.1 GeV respectively. The asymmetric shape (larger tail at low mass) comes mainly from events with at least one converted photon (electron energy loss by bremsstrahlung in the material ahead of the calorimeter). The energy scale and resolution systematic uncertainties are propagated to the mean and width parameters of the gaussian core of the double-sided Crystal Ball function.

### III.2.4.2 Background modelling

The diphoton background consists of three components: i) the irreducible  $\gamma\gamma$  background, ii) the  $\gamma$ -jet background and iii) the jet-jet background (with one or two jets faking photons for the two last components). Because of the total background smoothness and thanks to the constraints from large sidebands around the peak, a data-driven parametric approach is used. The background model is determined from studies of the signal yield bias in signal+background fits performed over high statistics background-only pseudo-data (the so-called spurious signal test). In order to select a function, the

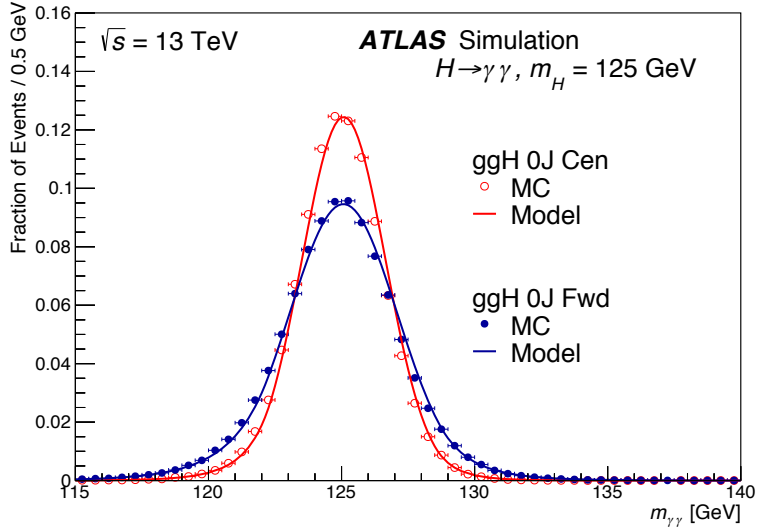


Figure 27: Diphoton mass signal shapes (simulated events and fit models) for two ggF categories [24].

associated spurious signal is required to be less than 10% of the expected signal yield or less than 20% of the expected statistical uncertainty. These pseudo-data need to be as similar as possible to the final data. For low rate categories, the simulation statistics is not sufficient and background-enriched control regions are used. For the other categories, the pseudo-data are built from a very high statistics  $\gamma\gamma$  fast simulation sample, reweighted by an  $m_{\gamma\gamma}$  linear function correcting for the shape difference between  $\gamma$ -jet, jet-jet and the  $\gamma\gamma$  reference. The  $\gamma$ -jet and jet-jet mass shapes are extracted in control regions where one (or two) photon(s) is (are) required to fail the identification or the isolation criteria. In addition to the shapes, the fractions of  $\gamma\gamma$ ,  $\gamma$ -jet and jet-jet background events need to be extracted: this is done using the so-called 2 $\times$ 2-D sideband method [25]. The Figure 28 shows the background decomposition in the inclusive case. The fractions of  $\gamma\gamma$ ,  $\gamma$ -jet and jet-jet background events are 79%, 19% and 3% respectively (the variations between reconstruction categories are quite small). At the end of the procedure, one of the most often selected background functions is an exponential of a second-order polynomial (2-parameter function).

### III.2.5 Systematic uncertainties

Many sources of systematic uncertainties need to be considered. Those uncertainties can be classified in three types:

- theory uncertainties, which affect the signal yields (some create migrations between truth bins)
- experimental uncertainties, which affect the signal yields and create migrations between reconstruction bins
- signal shape uncertainties
- background shape uncertainties.

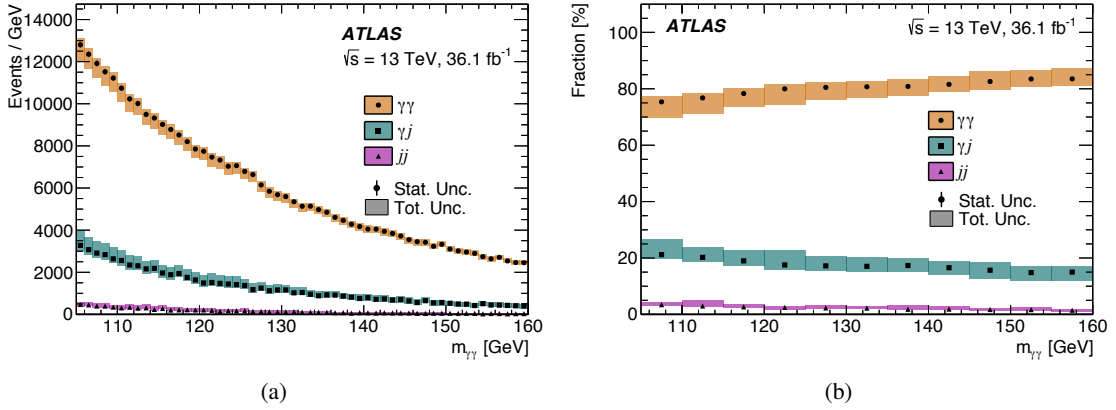


Figure 28: (a) Data-driven background decomposition: event yields (a) and (b) event fractions for  $\gamma\gamma$ ,  $\gamma j$  and  $j j$  events as a function of  $m_{\gamma\gamma}$  [24].

The Table 6 summarizes the full set of systematic uncertainties, with their typical impact on the simplified template cross sections (value or range of values) : in total, 205 nuisance parameters are considered in the fit.

### III.2.6 Statistical model

The parameters of interest are measured through a simultaneous unbinned maximum-likelihood fit of the 31 invariant mass spectra. The diphoton invariant mass range used is 105-160 GeV; this is the best compromise between a too short range which does not provide a good background control and a too large range which generates a large uncertainty associated to the background parametrization choice. The likelihood is built from the product of the reconstruction category likelihoods, which are marked probability Poisson distributions:

$$\mathcal{L}_i = \text{Pois}(n_i | N_i(\boldsymbol{\theta})) \cdot \prod_{j=1}^{n_i} f_i(m_{\gamma\gamma}^j, \boldsymbol{\theta}) \cdot G(\boldsymbol{\theta}),$$

where:

- $n_i$  ( $N_i$ ) is the observed (expected) number of selected candidates in the category  $i$ .  $N_i$  is given by:

$$N_i = (N_i^{\text{sig}} + N_i^{\text{spur}} \cdot \theta_i^{\text{spur}}) + N_i^{\text{bkg}}$$

with  $N_i^{\text{sig}}$  ( $N_i^{\text{bkg}}$ ) the expected signal (background) yield and  $N_i^{\text{spur}} \cdot \theta_i^{\text{spur}}$  the spurious signal yield

- $f_i(m_{\gamma\gamma}^j)$  is the value of the probability density function (pdf) of the invariant mass distribution evaluated for each candidate  $j$
- $\boldsymbol{\theta}$  represents the full set of nuisance parameters
- $G(\boldsymbol{\theta})$  is a global constraint term (penalty term associated to the pull of the nuisance parameters, which come from auxiliary measurements).

	Systematic uncertainty source	$N_{\text{NP}}$	Impact	Production mode	
Theory	ggH QCD	9	4%	VBF	
	PDF	30	1.5%	ALL	
	$\alpha_S$	1	1.5%	ALL	
	UE/PS	5	1.5%	ALL	
Experimental	Yield	Heavy flavor content	1	3%	ttH
		Luminosity	1	3.2%	ALL
		Trigger	1	0.4%	ALL
		Photon identification	1	1.6%	ALL
		Photon isolation	2	0.8%	ALL
	Migration	Flavor tagging	14	3%	ttH
		Jet	20	3 – 15%	VBF
		Jet flavor composition	7	6%	ttH
		Jet flavor response	7	1%	ttH
		Electron	3	0.6%	VH
		Muon	11	0.5%	VH
		Missing transverse momentum	3	4 – 5%	VH
		Pileup	1	1 – 6%	ggF
		Photon energy scale	40	0.2 – 2%	ALL
Mass	ATLAS-CMS $m_H$	1	< 0.1%	ALL	
	Photon energy scale	40	< 0.1%	ALL	
	Photon energy resolution	9	3%	ALL	
Background	Spurious signal	31	3%	ALL	

Table 6: Summary of the considered sources of systematic uncertainties and range of their impact (expected yield variation or migration) for the relevant categories (adapted from [24]). The production mode whose measurement is the most affected is mentioned for each source.

The systematic uncertainties affecting the signal yield and the mass resolution are incorporated into the likelihood via log-normal constraints (as these are cases where negative values are unphysical), while gaussian constraints are used for the mass scale and the spurious signal. The measurement is performed using the profile likelihood ratio test statistic, defined as:

$$\Lambda(\nu) = -2 \ln \frac{\mathcal{L}(\nu, \hat{\theta}_\nu)}{\mathcal{L}(\hat{\nu}, \hat{\theta})}, \quad (1)$$

where  $\nu$  represents the full set of measured parameter of interest,  $\hat{\nu}$  and  $\hat{\theta}$  are the values of the parameter of interest and nuisance parameters that unconditionally maximize the likelihood (the ‘absolute maximum’) and  $\hat{\theta}_\nu$  are the values of the nuisance parameters that maximize the likelihood on the condition that  $\nu$  is measured (profiling of nuisance parameters). In the asymptotic approximation,  $\Lambda(\nu) = 1$  provides the  $1\text{-}\sigma$  uncertainty interval. Specific uncertainty components (theory, experimental and statistical) can be determined by fixing the other nuisance parameters to their best-fit values and by doing a quadrature subtraction from the total uncertainty.

### III.3 Results

#### III.3.1 Observed data

The 31 diphoton invariant mass distributions (corresponding to the reconstruction categories) are used in the fit; for illustration purposes, the Figure 29 shows the sums of the distributions of the categories relevant for each production mode, displaying both the fitted signal and background components.

#### III.3.2 Simplified template cross sections

Because of the limited sensitivity of the current dataset, 9 simplified template cross sections, defined by merging phase space regions of the stage-1 scheme as described in Section III.1.2, are measured. In the likelihood, the signal yield  $N_{\text{sig}}^i$  in each reconstruction category  $i$  is defined as:

$$N_{\text{sig}}^i = \sum_t N_{\text{sig},t}^i = \sum_t \int L dt \times \sigma_r \times B^{\text{SM}}(H \rightarrow \gamma\gamma) \times \epsilon_t^i$$

where:

- $\sigma_r$  are the 9 simplified template cross sections to be measured (these are the parameters of interest).
- $\epsilon_t^i$  is the probability that an event in the phase space region  $t$  gets reconstructed and selected in the reconstruction category  $i$ . It is determined from MC as the ratio of the expected number of events in the reconstruction category  $i$  coming from the phase space region  $t$  to the total number of expected events in the phase space region  $t$ .

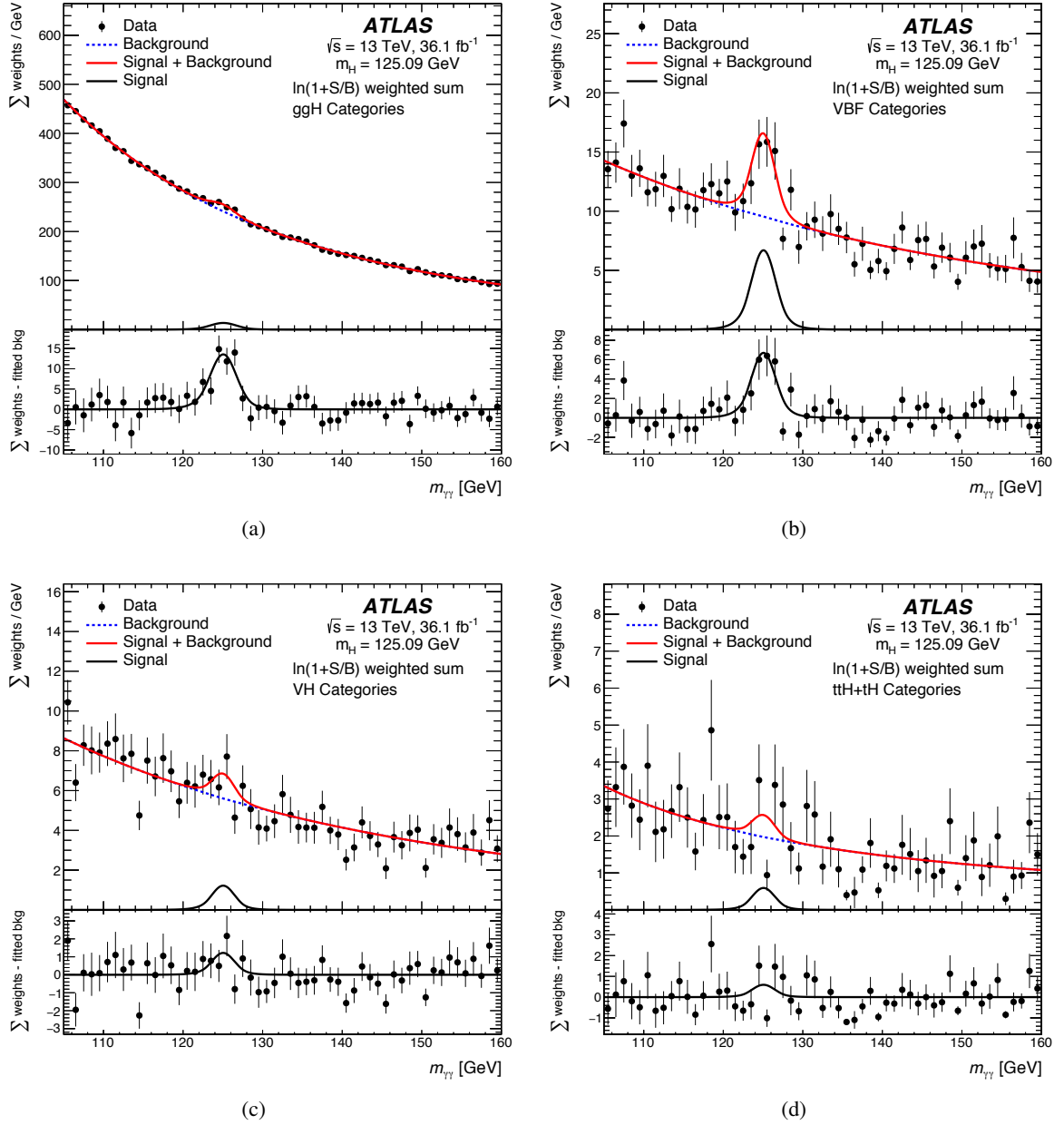


Figure 29: Weighted (from the expected signal to background ratio in each category) diphoton invariant mass spectra observed in the 13 TeV data for events belonging to: (a) ggF categories (b) VBF categories, (c)  $VH$  categories and (d)  $t\bar{t}H$  categories [24]. The bottom inserts show the residuals between the data and the background component of the fitted model.

Measurement region ( $ y_H  < 2.5$ )	Result	Uncertainty			SM prediction
		Total	Stat.	Syst.	
ggH, 0 jet	37	$^{+16}_{-15}$	( $\pm 14$ )	$^{+6}_{-5}$ fb	$63 \pm 5$ fb
ggH, 1 jet, $p_T^H < 60$ GeV	13	$^{+13}_{-12}$	( $\pm 12$ )	$^{+5}_{-4}$ fb	$15 \pm 2$ fb
ggH, 1 jet, $60 \leq p_T^H < 120$ GeV	5	$\pm 6$	( $\pm 6$ )	$^{+2}_{-1}$ fb	$10 \pm 2$ fb
ggH, 1 jet, $120 \leq p_T^H < 200$ GeV	2.8	$^{+1.7}_{-1.6}$	( $+1.6$ $-1.5$ )	$^{+0.7}_{-0.5}$ fb	$1.7 \pm 0.3$ fb
ggH, $\geq 2$ jet	20	$^{+9}_{-8}$	( $\pm 8$ )	$^{+4}_{-3}$ fb	$11 \pm 2$ fb
$qq \rightarrow Hqq, p_T^j < 200$ GeV	15	$^{+6}_{-5}$	( $\pm 5$ )	$^{+3}_{-2}$ fb	$10 \pm 0.5$ fb
ggH + $qq \rightarrow Hqq$ , BSM – like	2.0	$\pm 1.4$	( $\pm 1.3$ )	$\pm 0.6$ fb	$1.8 \pm 0.4$ fb
VH, leptonic	0.7	$^{+1.4}_{-1.3}$	( $+1.4$ $-1.2$ )	$^{+0.4}_{-0.3}$ fb	$1.4 \pm 0.1$ fb
Top	0.7	$^{+0.8}_{-0.7}$	( $+0.8$ $-0.7$ )	$^{+0.2}_{-0.1}$ fb	$1.3 \pm 0.1$ fb

Table 7: Measured simplified template cross sections times branching ratio [24]. The SM predictions [6] are shown for each region.

The measured cross sections are given in Table 7: all results are in agreement with the Standard Model values. The largest deviation ( $1.7\sigma$ ) is found in the ggF (0 jet) category. In spite of the merging scheme used, the measurements are still statistically limited (the statistical uncertainty represents typically 80% or more of the total uncertainty). Because of the non-perfect purity of the reconstruction categories (several truth bins contribute to one reconstruction category), the measured cross sections are correlated; the measured correlations are shown in Figure 30. The largest correlation is observed between the  $qq \rightarrow Hqq, p_T^j < 200$  GeV category and the ggH,  $\geq 2$  jet category: this comes from the relatively large selection efficiency of such ggF events in the VBF reconstruction categories. 95% CL limits are set in the BSM-like category (sensitive in particular to a boosted  $V(\rightarrow jj)H$  contribution): the observed limit is 4.4 fb (the measured cross section is 2.0 fb).

### III.3.3 Other results

#### III.3.3.1 Production mode signal strengths

The inclusive signal strength is the ratio of the measured total Higgs boson production cross section times branching ratio to the SM prediction; production mode signal strengths are defined in a similar way. Because of the limited sensitivity to rare production modes, the measurement is performed under the following assumptions:

- $\mu_{VH} = \mu_{ZH} = \mu_{WH}$
- $\mu_{bbH} = \mu_{ggH}$
- the  $tH$  and  $t\bar{t}H$  productions are measured together ( $\mu_{top} = \mu_{t\bar{t}H+tH}$ ).

The results are presented in Figure 31. It can be noted that the VBF signal strength is  $2.2\sigma$  above the SM prediction. Such a large deviation is not observed in the VBF truth bin of the STXS results ( $\sim 1\sigma$  excess, see Table 7); but the ggH,  $\geq 2$  jet region also shows a  $\sim 1\sigma$  excess. Both excesses

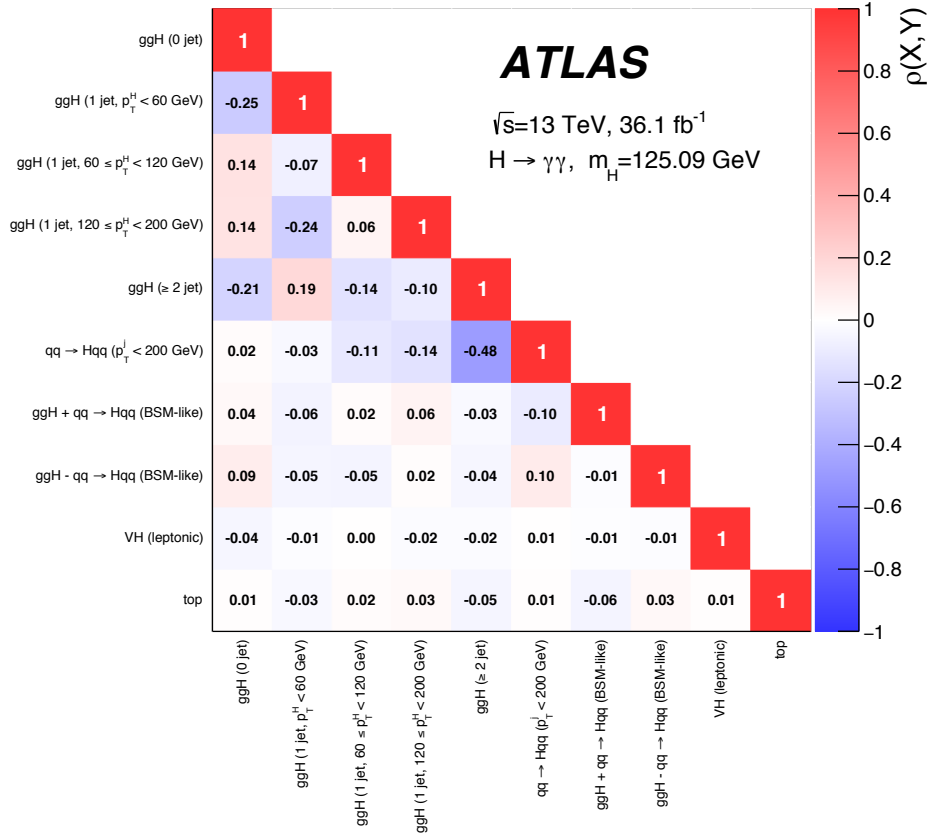


Figure 30: Observed correlations between the measured simplified template cross sections (including both the statistical and systematic uncertainties) [24].

are measured simultaneously in the signal strength case, ignoring the kinematic differences between these contributions. This example illustrates nicely how the simplified template cross section approach provides more information for further interpretations of the experimental results.

### III.3.3.2 $\kappa$ -fit

The  $\kappa$ -framework is described in Section I.2.2.

#### BSM particles in the loops

To describe the loop processes in the ggF production mode and in the  $H \rightarrow \gamma\gamma$  decay, effective coupling-strength modifiers are introduced (the loops are not resolved in terms of the fundamental modifiers):

Assuming all other couplings to their SM value (this assumption is approximately valid only for small deviations of  $\kappa_g$  or  $\kappa_\gamma$ ), a 2-D scan is performed: the 68% and 95% CL two-dimensional contours are shown in Figure 32 (a). The central values are:  $\kappa_g = 0.76_{-0.14}^{+0.17}$  and  $\kappa_\gamma = 1.16_{-0.14}^{+0.14}$ .

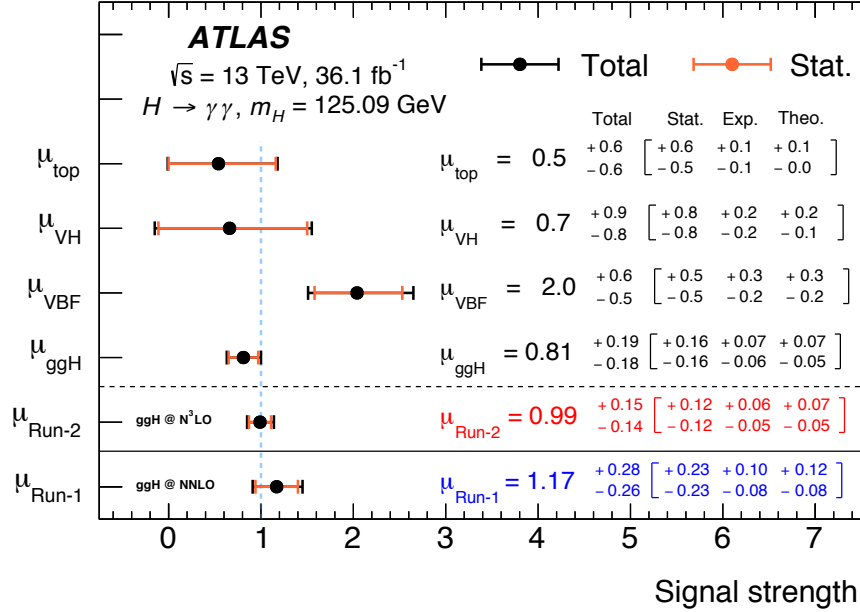


Figure 31: Summary of the signal strengths measured for the different production processes (ggH, VBF, VH and top) and globally ( $\mu_{\text{Run-2}}$ ) [24]. The global signal strength measured at 7 and 8 TeV ( $\mu_{\text{Run-1}}$ ) is also shown [26].

### Relative sign between the vector and top couplings

The experimental observables are not sensitive to the absolute sign of the couplings; the relative sign between different couplings can only be probed through interference effects. In particular, any sensitivity to the relative sign between vector and top couplings can only come from the  $H \rightarrow \gamma\gamma$  decay (via the  $W$ - $t$  interference) or from the ggZH or tH production (via respectively the  $Z$ - $t$  interference and the  $W$ - $t$  interference). Only the latter case plays a role when considering only the  $\gamma\gamma$  decay. In order to probe this relative sign, a three-ratio model is considered, based on:  $\kappa_{g\gamma} = \kappa_g \kappa_\gamma / \kappa_H$ ,  $\lambda_{Vg} = \kappa_V / \kappa_g$ , and  $\lambda_{tg} = \kappa_t / \kappa_g$  ( $\lambda_{tg}$  is allowed to be negative). The measured values are:  $\kappa_{g\gamma} = 0.90 \pm 0.10$ ,  $\lambda_{Vg} = 1.41^{+0.31}_{-0.26}$  and  $\lambda_{tg} = 0.8^{+0.4}_{-0.6}$ . The Figure 32 (b) shows the likelihood profile for the measurement of  $\lambda_{tg}$ . The current sensitivity to the sign is rather limited (less than 1-sigma).

## III.4 Contributions

- Diphoton Background Modeling Task Force (2016)

I was convener of this task force, which was transverse to several analyses with a diphoton final state. The main focus was on the development of common strategies for the Run 2 high statistics challenges (trying to find alternatives to the spurious signal method) and on the fake photon modelling by the simulation (as large data/MC disagreements are observed.)

- Simplified template cross sections

I performed studies in the very early phase to optimize the truth/reconstruction category definition and provided feedback to the Higgs LHC working group.

I implemented for ATLAS in the derivation framework a common ATLAS-CMS truth-level categorization tool (based on Rivet [27]).

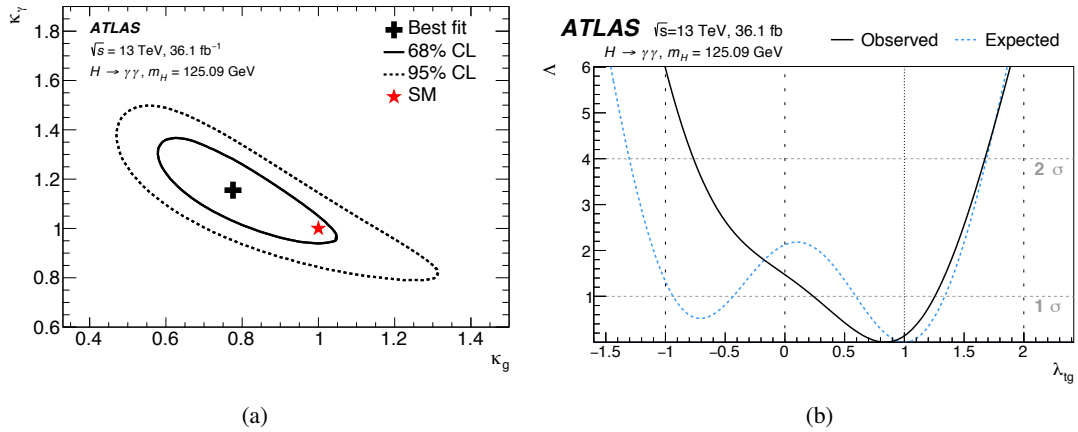


Figure 32: (a) Likelihood contour in the  $(\kappa_g, \kappa_\gamma)$  plane compared to the Standard Model prediction (red star) [24]. (b) Likelihood profile of the observed and expected coupling-strength modifier ratio  $\lambda_{tg}$  [24].

I currently supervise, as PhD supervisor, the work of Saskia Falke on the statistical model and the optimization of VBF categories for the full Run 2 result (exploring in particular the possible use of the quark/gluon jet tagging).

I currently supervise the ongoing work of Oleh Kivernyk (postdoctorant at LAPP) on VBF theory uncertainties (evaluation of uncertainties in a new scheme developed to treat consistently the uncertainties between truth bins).

- Mass analysis (not discussed here but performed synchronously in the coupling working group)  
I supervised the work of Saskia Falke on the background and signal uncertainties, the impact of calibration systematics and category optimization studies.
- Photon identification  
I supervised the work of Oleh Kivernyk on the re-tuning of the tight photon identification menu (re-tuning required to increase the pileup robustness and maintain a high efficiency).

## Part IV

# Higgs boson prospects with future colliders: from 2020 to 2050

*This chapter discusses the possible prospects for the Higgs boson physics over the next decades, considering the possible options for future colliders. Some short-term commitments along this open road are presented, as well as some longer-term work paths, both on the calorimetry and Higgs boson sides.*

### IV.1 Introduction

I began my research career in the starting phase of the LHC machine during ATLAS commissioning in 2006 (while it was a 20-year old project), and then pursued during the final exploitation phase of the Tevatron accelerator. Given this privilege, I have not contributed to the area of activities covering the long pre-running experiment phase: from the R&D on detection techniques to a detector design, prototype, construction and installation. But this is really what builds the future of high energy physics; for this reason, I am starting to lean my research towards more detector instrumentation activities.

This project part is structured as follows. First the open options for future colliders are reviewed; in the coming years, major decisions will have to be made (e.g. update of the European Strategy for Particle Physics in 2020). Then I will describe my ramping-up activities for the ATLAS LAr calorimeter electronics upgrade, and discuss quickly the challenges for the design of calorimeters in future experiments. Finally, I will present the potential for discoveries in the Higgs boson sector.

### IV.2 Future colliders at the energy frontier: what is next?

#### IV.2.1 The high luminosity LHC program

The integrated luminosity design goal of the High Luminosity LHC (HL-LHC) program is an increase of a factor ten with respect to the LHC first phase goal (reachable thanks to an increase by a factor 5-7 of the instantaneous luminosity with respect to the nominal value):  $3000 \text{ fb}^{-1}$  should be collected by 2037 (see Figure 33). This comes at the price of a very high pileup, up to 200. To reach such performance, many technical upgrades are required, including in particular:

- 12 quadrupoles built in niobium-tin ( $\text{Nb}_3\text{Sn}$ ), reaching a peak magnetic field strength of about 12 T, to squeeze the beams;
- 8 crab cavities to tilt the proton bunches in each beam just before collision (making them collide almost head-on);
- 20 new collimators to reinforce machine protection (higher total beam energy);

- long high-power superconducting links with almost zero energy dissipation to carry current to the magnets.

This represents a system upgrade over 1.2 km of the LHC ring. Final prototypes are being developed and tested, before moving towards the production and the installation in 2024-2025.

The HL-LHC program was considered as the highest priority in the last update of the European Strategy for Particle Physics (2014) and has been approved by the CERN Council. The options for other future linear or circular accelerators ( $e^+e^-$  or  $pp$ ) at the energy frontier are discussed in the next sections: no decision has been taken yet, and this represents the key challenge for the coming update of the European Strategy for Particle Physics (2020).

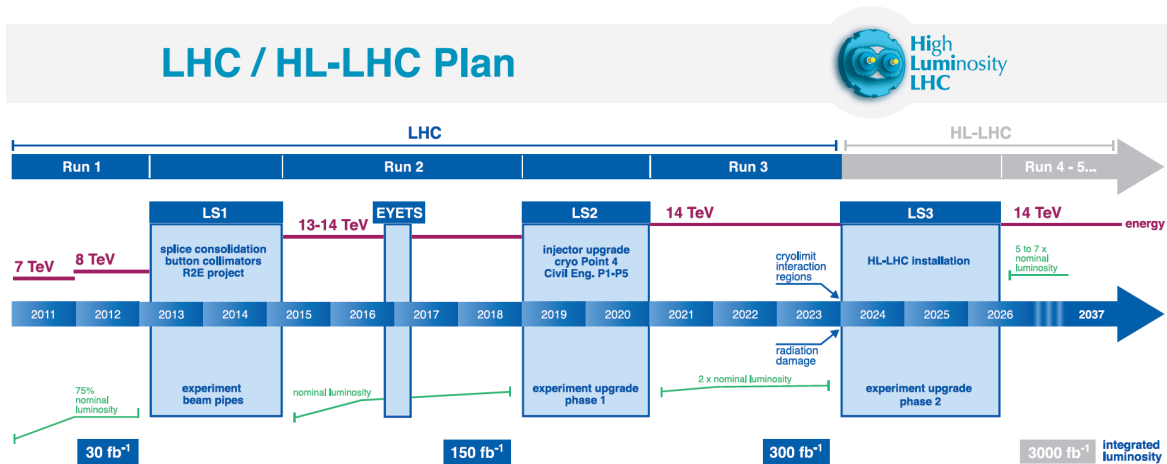


Figure 33: Long-term planning of the HL-LHC program.

## IV.2.2 Linear colliders

The Technical Design Report of the International Linear Collider (ILC) project was published in 2013 [28]: the baseline scenario consists of a linear electron-positron collider at 500 GeV (center-of-mass energy) built in a 11-km long tunnel (see Figure 46). The acceleration system is based on 16000 1 m-long superconducting radiofrequency cavities made of pure niobium with a gradient up to 35 MV/m. A system with two movable detectors (the so-called push-pull technique) is envisioned (one detector is taking data while the second one can be serviced). Some key aspects are:

- The design luminosity is  $2 \cdot 10^{34} \text{ cm}^{-2}\text{s}^{-1}$ .
- The energy of the beam is tunable, allowing precise energy scans.
- The beams can be polarized: up to 80% for the electron beam and up to 30% for the positron beam.

The most recent proposal (2017) is to build a 250-GeV machine (Higgs factory), as a first stage and keeping the energy upgradability advantage inherent to a linear collider. The price estimate of such a machine is 5 billion \$ (40% less than the baseline scenario). Technically, the project is ready to go; the ILC accelerating technique was in particular validated by the success of the X-Ray Free-Electron

Laser (XFEL) project, which is a 2-km long accelerating facility in DESY. A firm decision by the Japan government, for the financial support of the project, is expected to be taken in 2018 or 2019. In the case of a positive decision, the earliest starting physics date is announced to be around 2030.

Another concept for a linear collider is the Compact Linear Collider (CLIC) project. Its initial design (started in 1985) aimed at a 3-TeV center-of-mass energy linear collider (in a 30-km long tunnel). This high beam energy and the high luminosity ( $6 \cdot 10^{34} \text{ cm}^{-2}\text{s}^{-1}$ ) goals required to work on the development of very high accelerating cavities (gradient up to 100 MV/m) and techniques allowing to reach nanometre beam size at the interaction point. In spite of promising results obtained in the CTF3 facility at CERN, the CLIC technology is not yet mature enough; for this reason, it does not benefit from the same opportunity window, of a Higgs precision facility complementary to the HL-LHC program.

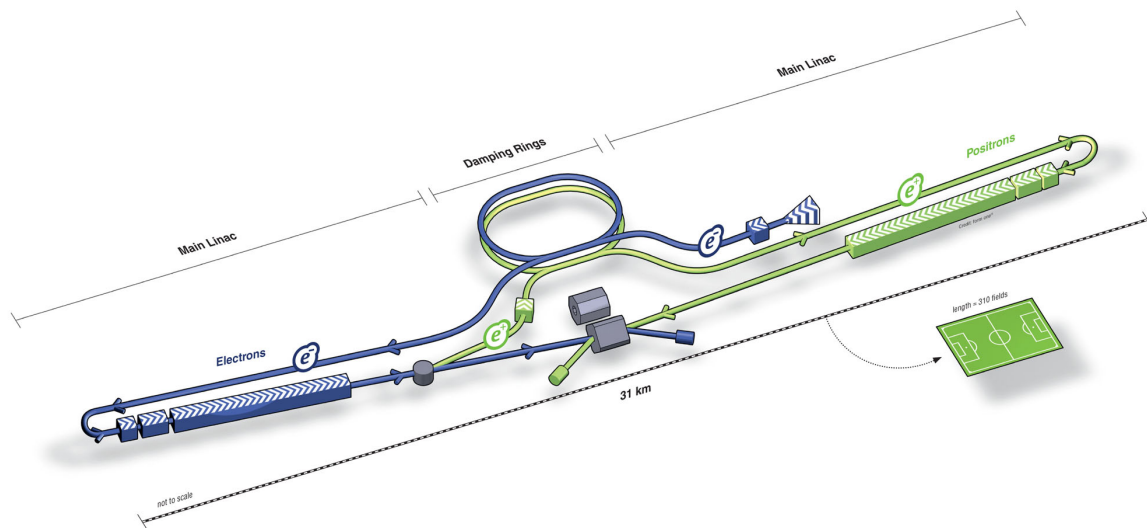


Figure 34: Schematic view of the ILC infrastructure.

## IV.2.3 Circular colliders

### IV.2.3.1 The FCC project

In order to prepare the post-LHC era, CERN launched in 2012 the Future Circular Collider (FCC) study. The baseline design is focused on a 100 TeV  $pp$  collider located in a 100 km tunnel in the CERN area (see Figure 35<sup>6</sup>). The key technological step is to develop 16 T superconducting magnets; a world-wide R&D program on  $\text{Nb}_3\text{Sn}$  dipoles is required to reach this goal. This program directly benefits from the HL-LHC developments. The design luminosity is  $5 \cdot 10^{34} \text{ cm}^{-2}\text{s}^{-1}$ ; this could be pushed up to  $25 \cdot 10^{34} \text{ cm}^{-2}\text{s}^{-1}$  in a later phase, producing up to 1000 pileup events.

<sup>6</sup> The LAPP would then be at  $\sim 10$  km of an experiment point, as it is planned to have two high luminosity experiments: one close to CERN and the other one on the opposite side of the ring, i.e. close to the Mandallaz mountain.

The FCC-hh (for hadron-hadron) project is accompanied by an electron-positron collider project (FCC-ee), which could be running in the same tunnel with a beam energy up to 200 GeV, prior to the hadron machine installation and operate as a  $W$ ,  $Z$ , Higgs and top factory. The possible schedule for the FCC project is shown in Figure 36. A complete Conceptual Design Report is being prepared and should be ready by the end of 2018.

To be complete, we should also mention the CEPC-SPPC project in China [CEPC\_TDR]; the concept is similar (the baseline design is a 54-km ring), starting from an electron-positron machine at 240 GeV and going in a second phase to a proton-proton collider at 50-100 TeV.

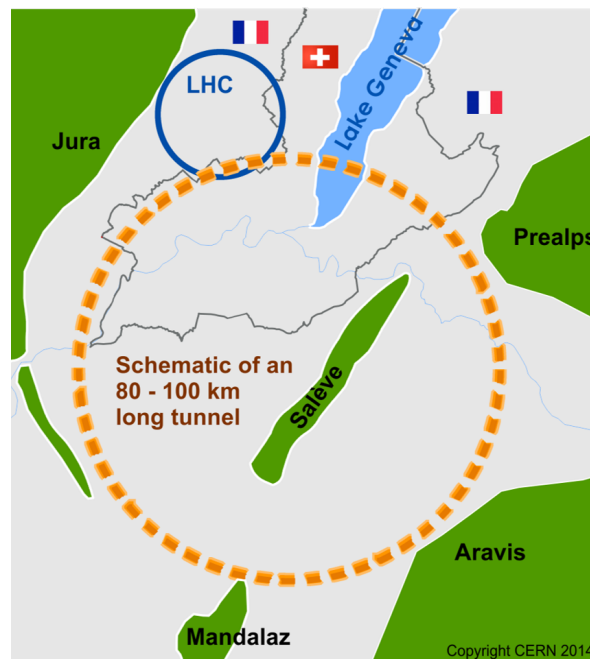


Figure 35: Schematic view of the FCC tunnel infrastructure.

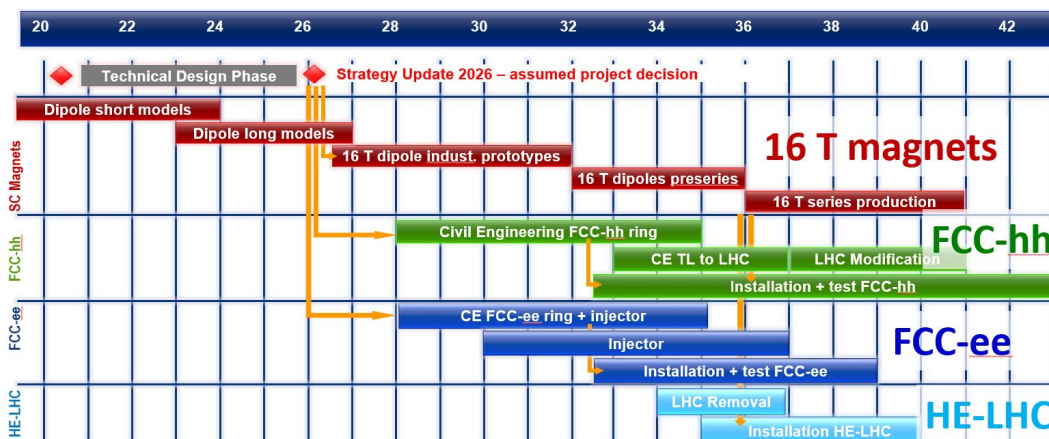


Figure 36: Possible schedule for the FCC project [29].

### IV.2.3.2 High energy LHC

Beyond HL-LHC, the possibility to increase the energy of the LHC by a factor 2 (leading to 27-TeV collisions) inside the same tunnel, is being studied. This requires also 16 T Nb<sub>3</sub>Sn dipoles, which are more compact and so even more challenging than the FCC-hh ones. While the idea to use the same tunnel might be appealing, the dipole challenges, the relatively modest increase of the high energy reach and the absence of an electron-positron program make the opportunities of this project not as vast. One advantage is the lower cost in comparison to other projects. On the physics side, one interesting aspect is the potentially large increase of the sensitivity for the Higgs boson self-coupling measurement (an extremely important direct probe of the Higgs boson potential) with respect to the HL-LHC sensitivity, a measurement whose sensitivity may be hardly on the edge of the SM rate at HL-LHC.

## IV.3 Calorimetry: from ATLAS upgrades to future experiments

### IV.3.1 The ATLAS LAr Phase-1 upgrade

#### IV.3.1.1 Physics requirements

The anticipated conditions for Run 3 (which were used as specifications for the design of the phase 1 upgrade components) are an instantaneous luminosity of  $L = 3 \cdot 10^{34} \text{ cm}^{-2}\text{s}^{-1}$  and an average number of interactions per bunch crossing  $\langle \mu \rangle = 80$ . The LAr phase 1 upgrade system has been designed in order to maintain L1 trigger thresholds similar to Run 2 (typically 15 kHz for a single electron L1 trigger at 30 GeV and 10 kHz for a missing transverse energy L1 trigger at 70 GeV) in these harsher conditions. This is mainly achieved via a new readout trigger chain based on so-called supercells (see Figure 37): the current trigger towers have a window size of  $0.1 \times 0.1$  and no longitudinal information, while the supercell energies are computed per layer and with a four times higher  $\eta$ -granularity for the front and middle layers. In addition, the digitization precision is improved by a factor 4 and the transverse energy is computed using an optimal filtering approach (instead of look-up tables in the current system). This improved readout allows:

- a higher background rejection for the same electron efficiency, thanks to the use of shower shape variables;
- sharper trigger turn-on curves;
- a better pileup subtraction.

#### IV.3.1.2 Overview of the upgrade system

The overall view of the upgraded system is shown in Figure 38. All the details can be found in Reference [30]. The key components are:

- the LAr Trigger Digitizer Board (LTDB), located on the detector;
- the LAr Digital Processing System (LDPS), located in crates in USA15.

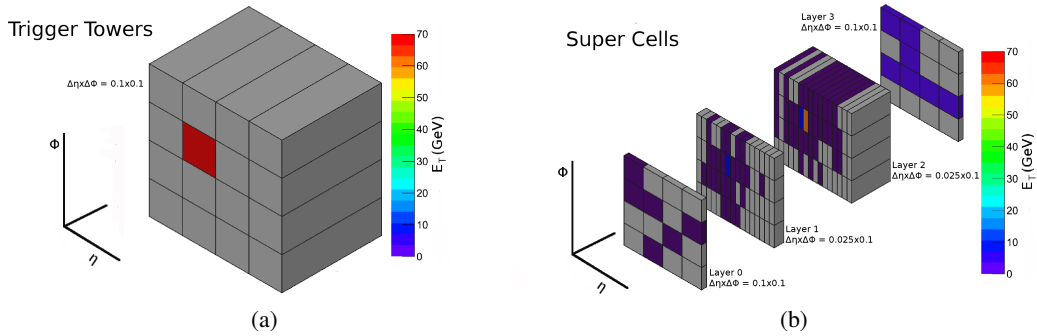


Figure 37: An electron (with 70 GeV of transverse energy) as seen (a) by the existing L1 calorimeter trigger electronics and (b) by the upgraded trigger electronics [30].

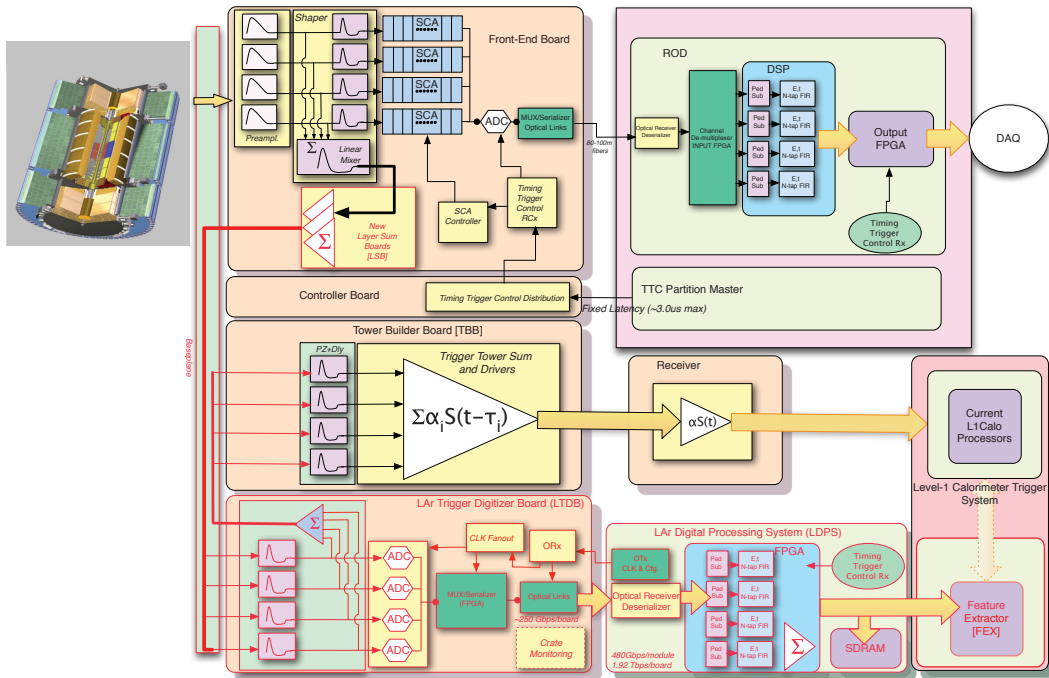


Figure 38: Schematic block diagram of the Phase-I upgrade LAr trigger readout architecture [30]. The new components are indicated by the red outlines and arrows.

The LAPP group has been involved in the LDPS from the initial design phase.

### IV.3.1.3 The LAr Digital Processing System

**Data flow in the backend system** The LDPS consists of an Advanced Telecom Computer Architecture (ATCA) carrier equipped with four Advanced Mezzanine Cards (AMC), called LATOME boards (for LAr Trigger prOcessing MEzzanine). The incoming/outgoing data flows around the LDPS are sketched in Figure 39. There are four main data paths:

- the ADC supercell data coming at 40 MHz from the LTDB;

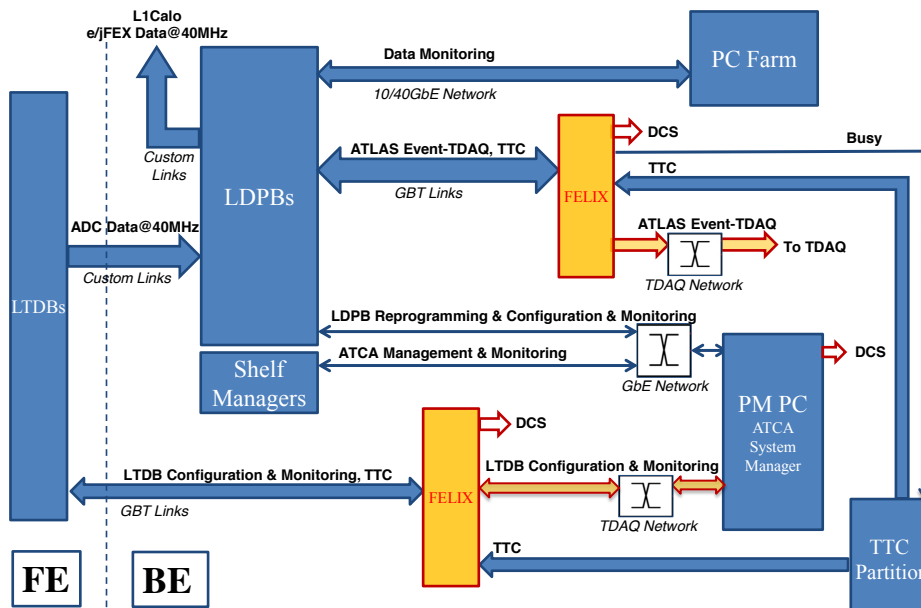


Figure 39: Schematic overview of the LDPS system [30]. The physical elements are represented as boxes and the links as arrows.

- the outgoing e/j-FEX (Feature EXtractor) data towards the L1 trigger system (supercell transverse energies computed on the LATOME) at 40 MHz (this is the main functionality of the new readout);
- the outgoing data towards the central ATLAS TDAQ system (upon a L1-accept trigger decision);
- the monitoring data going to a dedicated PC via a 10 GbE link.

**The LATOME boards** The basic structure of the LATOME board (developed at LAPP) consists of a 16-layer PCB, designed around the processing FPGA (ALTERA Arria 10). Figure 40 (a) shows the bare LATOME board, where many components can be seen (external memories, DC/DC alimentations, clocks, etc.). Figure 40 (b) shows the LATOME board equipped with heatsinks, ribbons of individual fibers and front panel connectors.

**Current status** Many tests at the Electronics Maintenance Facility (EMF) at CERN have been performed in 2017 to validate the various functionalities of the LDPB, in particular the various blocks of the complex LATOME firmware (remapping, user code, monitoring, etc.). Recently, the power consumption and temperature limits were checked in real conditions (three carriers mounted in a crate with four LATOME running on each carrier). The ATLAS Production Readiness Review (which gives the green light to launch the production) for the backend system was successfully passed in March 2018, validating the so-called v3 version of the LATOME for production. Two such boards will be installed in ATLAS for the 2018 data-taking (replacing a previous version of the upgrade



at EMF in time before the installation in USA15.

Since September 2017, my LAr Phase-1 activities have ramped up significantly: I have worked on the preparation of the database for the tests of the production series, the optimization of the baseline correction algorithm for the FPGA and the elaboration of the schedule for the tests with LAPP engineers. I will participate to the tests of the LATOME boards at LAPP and take responsibilities for this phase; the preparation of the test bench at LAPP and of the test automatization procedure has started. Then I will continue my involvement up to the commissioning of the system. This activity will be my priority for the 2018-2021 period. I consider defining in this area a technical project which could constitute a part of a PhD thesis, for instance on the optimization and validation of the baseline correction algorithm for Run 3.

## **IV.3.2 The ATLAS LAr Phase-2 upgrade**

### **IV.3.2.1 Overview of the upgrade system**

The need to upgrade the LAr electronics for the HL-LHC phase readout is driven by:

- the ageing of the current electronics (the current system would need to work reliably for at least 10 more years);
- the limited radiation tolerance of the front-end boards (FEB) for the planned integrated luminosity. The criterion used for the qualification of the ASIC of the current FEB was a factor two smaller than the estimated total ionization dose for 3000-4000 fb<sup>-1</sup>;
- the incompatibility with the future trigger system (too small pipelines for data buffering);
- the too small dynamic range.

While the Phase-1 upgrade focuses on the trigger readout chain, the Phase-2 upgrade is a major upgrade of all the LAr main electronics readout: the front-end part and the back-end part will be fully upgraded with new boards. All the details can be found in Reference [31].

### **IV.3.2.2 The LAr Signal Processors**

The future LAr Signal Processors (LASP) boards of the backend system will replace the current Readout Driver (ROD) system (see the box labelled 'ROD' on Figure 38). These boards will receive the ADC values in two gains for all calorimeter cells at 40 MHz. The LASP will compute the energy via the OFC method and transmit the information to the data acquisition system (data flow of ~ 20 Gb/s), but also to the future Global Event Trigger Processors (for a reduced set of cells, above an energy threshold). The main building block of the LASP system is the FPGA processing unit; two FPGA will be mounted on an ATCA blade (see Figure 41). Two designs are under study: a monolithic approach or a two-mezzanine approach (similar design as the Phase-1 upgrade).

The LAPP is currently involved in the specifications and design phase of the LASP. Once the Phase-1 upgrade is behind us, I will join these efforts in a period which should correspond to the test phase of

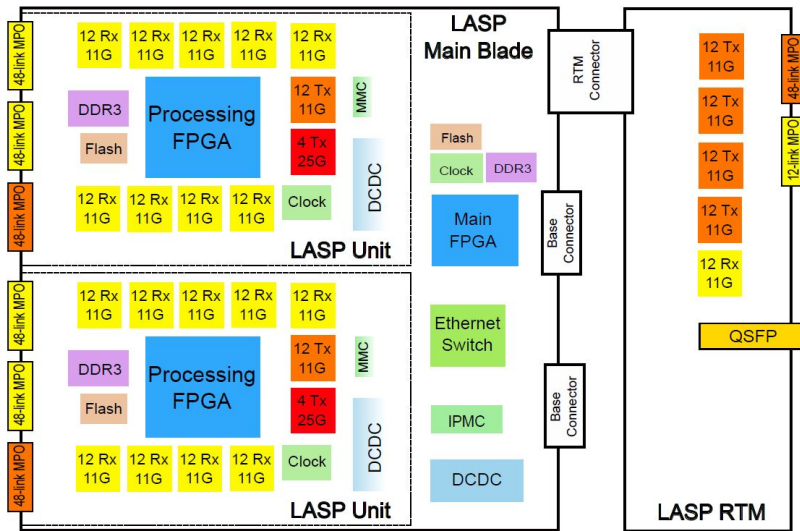


Figure 41: Layout overview of a LASP module [31].

the pre-production series, trying to make the best use of my Phase-1 experience. At this stage, a task sharing between the institutes involved in the project has not yet been defined.

### IV.3.3 Beyond HL-LC

Considering calorimeters in experiments at future colliders, the situation is very different between the ILC case and the FCC case. For ILC, two detector designs reached the Detector Design Report step already in 2013 [32]: the International Large Detector and the Silicon Detector. The main difference between the designs concerns the tracker, the calorimeter R&D (towards highly granular calorimeters optimized for the particle flow algorithm) is performed in a unique collaboration (CALICE). The most advanced option for the electromagnetic part is a 30-layer Silicon-Tungsten sampling calorimeter. While the requirements at FCC-ee are quite similar to the ILC ones, the requirements in the harsh conditions at FCC-hh are very different; in this section, I will discuss briefly the particular case of the electromagnetic calorimeter at FCC-hh.

A Conceptual Design Report (CDR) for all parts of the FCC project (accelerator, detectors and physics) should be ready by the end of the year 2018. The general structure of a possible detector layout is shown in Figure 42. Several requirements are similar to the ones which drove the design of the ATLAS and CMS electromagnetic calorimeters, but similar performance need to be reached in much harsher conditions. Some specific constraints are:

- the ability to reconstruct resonances up to  $\sim 40$  TeV (the depth needs to be at least  $30 X_0$ );
- the much higher pileup (up to  $\langle \mu \rangle = 1000$ );
- the high radiation dose, particularly in the forward region (the calorimeter coverage could go up to  $\eta = 6$ );
- the better timing resolution required (the bunch spacing could be 5 ns).

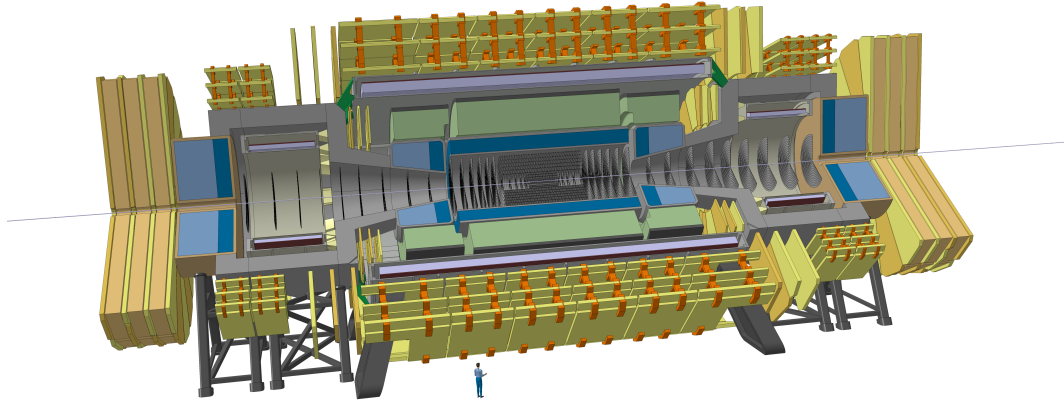


Figure 42: Overall view of a possible detector layout at FCC-hh.

One envisioned option for the electromagnetic part is the LAr/Pb technology used in ATLAS, with a 10 times higher granularity (see Reference [33]). Digital options are also considered, outside the forward region (see Reference [34]). It is clear that, at this stage, the main goal is to show that detectors, satisfying the physics requirements, could operate in the demanding conditions of FCC-hh.

The ILC timeline shows that the detector design cannot wait for the green light marking the start of the accelerator building. Currently, CNRS is involved in the FCC project only on the accelerator side. This is, in my view, not sufficient given the importance of such a project for the future of our field. I plan to contact FCC-hh detector working group members (probably after the CDR period); this will be a first step, to see how some efforts could be structured at the laboratory or institute level.

## IV.4 Potential for new discoveries in the Higgs boson sector

### IV.4.1 The precision quest

Many BSM scenarios predict Higgs couplings different from the SM values. The size and the pattern of the predicted deviations depend on the considered scenario, but a good rule of thumb is that deviations are of the order of  $\mathcal{O}(\frac{\nu^2}{M^2}) \sim 6\% \mathcal{O}(\frac{1 \text{ TeV}}{M})^2$ , where  $M$  is the scale of the new physics effects. This is for instance the case for non-SM particles contributing via loops to the  $gg \rightarrow H$  production or  $H \rightarrow \gamma\gamma$  decay, thus altering the effective gluon or photon coupling. In addition, to be sensitive at the  $3\sigma$ -level for a deviation  $\delta$ , the accuracy needs to be at the level of  $\delta/3$ ; considering a 1 TeV new physics scale, this requires a 2% accuracy on the relevant coupling.

A detailed study of the deviations predicted by different BSM scenarios is beyond the scope of this manuscript. The Table 43 summarizes the deviations for several classes of models [35]. The pattern of deviations is a key aspect to discriminate between different models.

Model	$\kappa_V$	$\kappa_b$	$\kappa_\gamma$
Singlet Mixing	$\sim 6\%$	$\sim 6\%$	$\sim 6\%$
2HDM	$\sim 1\%$	$\sim 10\%$	$\sim 1\%$
Decoupling MSSM	$\sim -0.0013\%$	$\sim 1.6\%$	$\sim -0.4\%$
Composite	$\sim -3\%$	$\sim -(3-9)\%$	$\sim -9\%$
Top Partner	$\sim -2\%$	$\sim -2\%$	$\sim +1\%$

Figure 43: Generic size of Higgs coupling deviations with respect Standard Model values, for various BSM scenarios, when all new particles are  $M \sim 1$  TeV (and mixing angles satisfy precision electroweak constraints in the relevant cases) [35].

## IV.4.2 Unexplored territories at Run 3

The integrated luminosity expected at Run 3 is  $\sim 300 \text{ fb}^{-1}$ , which represents a factor 2 increase with respect to Run 2. Given this relatively modest increase of the statistical power, one priority to maximize the Run 3 physics output is to prepare analyses for searches of rare or exotic Higgs boson decays which have not been performed so far. In this context, the search for the Higgs boson decay to one photon and one so-called dark photon is of particular interest<sup>7</sup>, while extremely challenging.

### IV.4.2.1 The Higgs boson as a dark matter portal

The absence of any clear signal for dark matter candidates so far reinforces the idea of a dark sector very weakly coupled the SM. It is possible that this dark sector has a rich internal structure and that it contains light or massless gauge bosons which mediate long-range interactions between the dark particles. One simple model is based on an unbroken U(1) gauge group, which predicts a dark photon  $\tilde{\gamma}$ ; in such a model, the Higgs boson decay to one photon and one dark photon, possible at loop level via heavy messengers, can be enhanced, with allowed values of the branching ratios up to  $\sim 5\%$  from current constraints [37]. This decay mode gives a clear signature from a high  $E_T$  photon and a high transverse missing energy (as the dark photon does not interact with ordinary matter), with a peak in the transverse mass distribution. Figure 44 illustrates this, for a parton-level analysis and an assumed branching ratio of 5%.

### IV.4.2.2 Feasibility in ATLAS

The real challenge of this search is the trigger; the single photon unscaled trigger signature has a threshold above 100 GeV and cannot be used. Thus a dedicated  $\gamma + E_T^{\text{miss}}$  trigger signature with thresholds around 40 GeV and a sufficient background rejection needs to be developed, exploiting the advantage of topological trigger signatures at L1 (available in ATLAS since the start of Run 2). The azimuthal angle between the leading jet direction and the  $E_T^{\text{miss}}$  direction is promising to reduce the dominant  $\gamma + \text{jet}$  background (entering the signal region from jet energy mis-measurements). With 100  $\text{fb}^{-1}$ , it is estimated that a signal could be observed (at the  $5\sigma$  level) for branching ratios as small as

<sup>7</sup> Analysis idea proposed by ATLAS colleagues of the Laboratoire de l'Accélérateur Linéaire in the context of the Photon-Portal ANR project [36] (in which I participate), but not performed at Run 2.

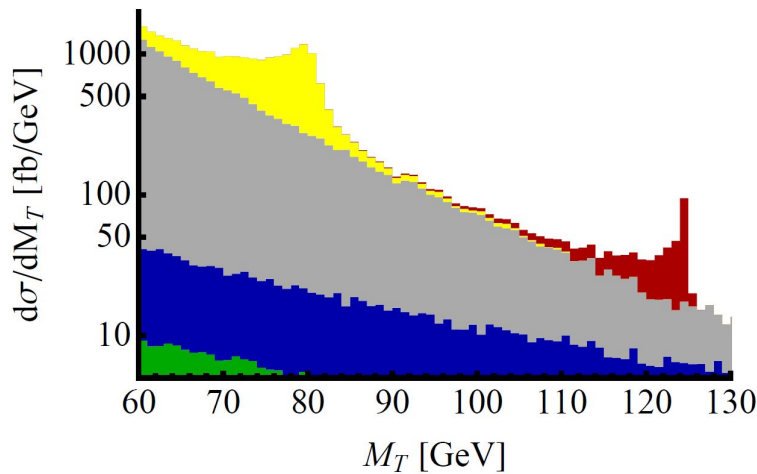


Figure 44: (a) The  $\gamma + E_T^{\text{miss}}$  transverse invariant mass distribution [37]. The signal is in red, and the dominant background is  $\gamma + \text{jet}$  in grey.

0.2% [38]. I consider defining a PhD project on this topic over the period 2019-2022; this time frame should allow to prepare the adequate trigger strategy and to exploit the first year of Run 3 data. Even if the sensitivity may not be as great as in the theory paper quoted before (because of an optimistic background estimation), this analysis would lead to the first direct limits on this branching ratio (well below the current constraints on the Higgs boson invisible decay). This may also lead to a fruitful collaboration with the theorists pushing to have such measurements performed at LHC as soon as possible.

#### IV.4.3 The potential at HL-LHC

Until 2030 or even 2035, the only Higgs factory available will be the HL-LHC. For this reason, even if it is now an approved project, to study its physics prospects in a realistic way is of primary importance; this is also required to strengthen the need for other complementary or surpassing facilities. Figure 45 summarizes the Higgs signal strength precision, for various final states, expected to be reached at HL-LHC for both ATLAS and CMS. These results date back to 2014, and it has to be mentioned that in some channels, the Run 2 results already obtained exceed the extrapolation for the full Run 3 statistics (thanks to the improvement of performance and/or analysis techniques). However, the global picture of the accuracy reachable remains largely valid.

The key task, to extrapolate to an integrated luminosity of  $3000 \text{ fb}^{-1}$  collected in HL-LHC conditions, is to estimate reliably the performance of the the Phase-2 upgraded detector (e.g. ITK for ATLAS) under high pileup condition ( $\langle \mu \rangle = 200$ ). The strategy is to derive smearing functions from fully simulated samples (including upgraded detectors), and to apply them at truth level on the relevant MC samples. The second important point is to estimate the possible evolution of the systematic uncertainties, which is critical for some channels. For ATLAS, the Run 1 experimental and theoretical systematic uncertainties are kept unchanged, only the statistical uncertainty is scaled. For CMS, the extrapolation is performed for the two following scenarios:

- Scenario 1 : unchanged systematic uncertainties;

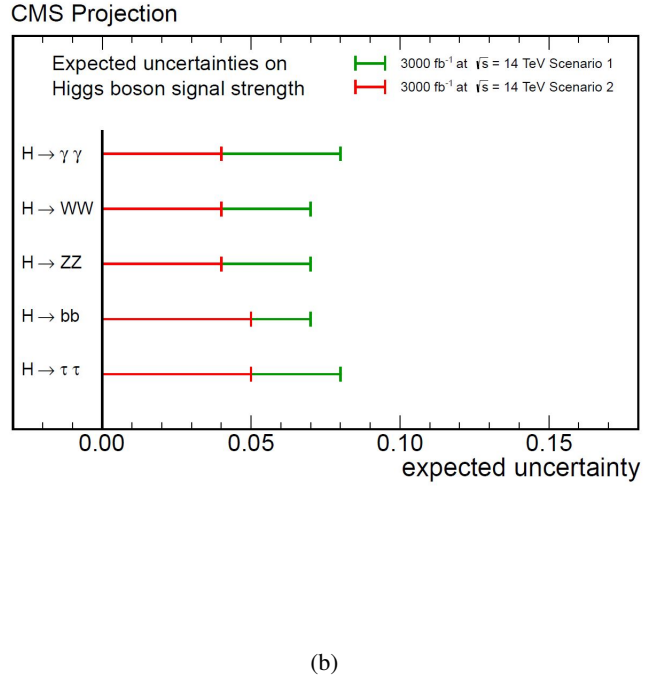
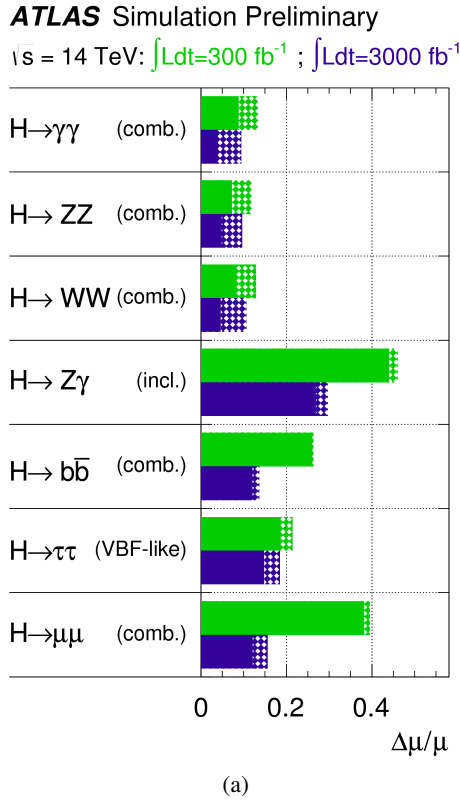


Figure 45: Relative uncertainty on the signal strength, for various Higgs final states, expected with  $3000 \text{ fb}^{-1}$  of 14 TeV HL-LHC data (a) for ATLAS [39] and (b) for CMS [35].

- Scenario 2 : experimental uncertainties scaled with luminosity and theory uncertainties halved.

Performing a  $\kappa$ -fit (without resolving the loops), the overall reached accuracy per experiment is typically 4 – 5% for the main couplings ( $\kappa_Z$ ,  $\kappa_W$ ,  $\kappa_\gamma$ ,  $\kappa_g$ ,  $\kappa_\tau$ ,  $\kappa_b$  and  $\kappa_t$ ) and 10 – 15% for rare processes ( $\kappa_\mu$  and  $\kappa_{Z\gamma}$ ).

#### IV.4.4 The ultimate precision

##### IV.4.4.1 The unique prospects at an electron-positron collider

The experimental conditions at an electron-positron collider favour by design precision measurements:

- a precisely known collision initial state (not the case at a hadron machine);
- a clean environment (absence of strong interaction backgrounds), allowing the use of highly granular detectors with advanced particle flow techniques;
- the possibility to have electron and positron beam polarization very well measured (a 0.1% precision on the luminosity-weighted average polarization could be reached). This allows to collect subsamples of data with different sensitivities for different processes.

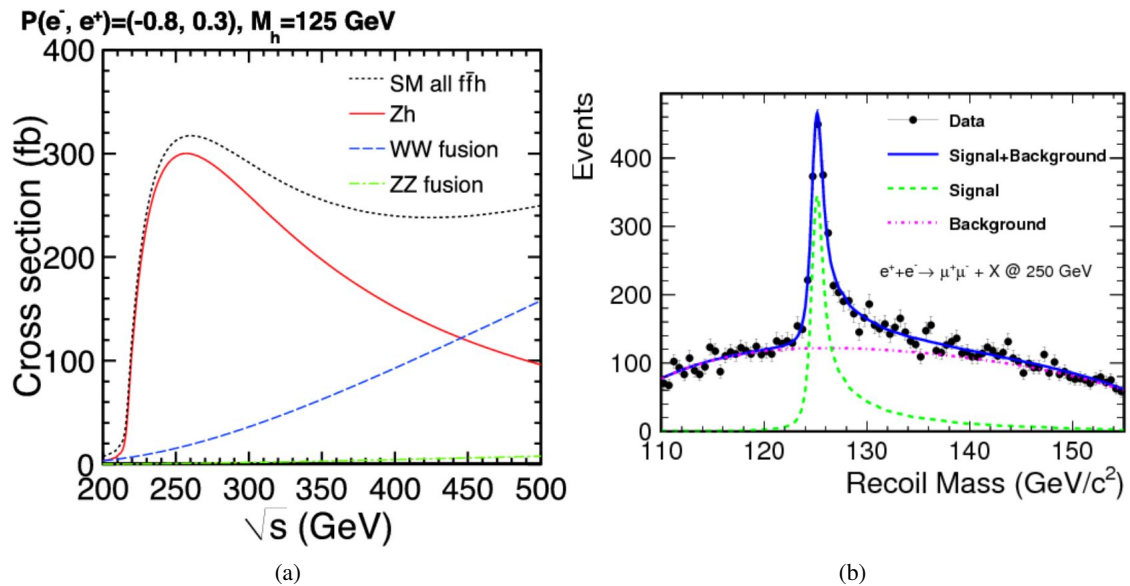


Figure 46: (a) Production cross section for  $ee \rightarrow ZH$ ,  $ee \rightarrow \nu\nu H$  and  $ee \rightarrow eeH$  processes as a function of the centre-of-mass energy for  $m_H = 125$  GeV [40]. (b) Recoil mass distribution in the  $Z \rightarrow \mu\mu$  case at  $\sqrt{s} = 250$  GeV [41].

At the ILC, there are three major Higgs production processes:  $ee \rightarrow ZH$  (Higgsstrahlung, largely dominant in the 250 GeV scenario),  $ee \rightarrow \nu\nu H$  ( $W$  fusion) and  $ee \rightarrow eeH$  ( $Z$  fusion). Figure 46 (a) shows the dependence of these cross sections with the centre-of-mass energy. The recoil mass technique (uniquely possible at an electron-positron collider) allows a precise measurement of the  $\sigma_{ZH}$  cross section, inclusively over all Higgs decay modes (including invisible decays); this is illustrated in Figure 46 (b), in the  $Z \rightarrow \mu\mu$  case. Considering a particular decay mode,  $\sigma_{ZH} \cdot BR$  is also measurable, providing an absolute branching ratio measurement. A particular case is the top coupling: the 250 GeV scenario does not offer access to the  $ee \rightarrow ttH$  process, the 500 GeV stage of the ILC is required. One asset of the ILC is that the total width is accessible in a completely model-independent manner, by combining several measurements and using in particular the relation  $\Gamma_H = \Gamma_{WW}/BR(H \rightarrow WW)$ .

The previous paragraph discusses the ILC case, but the circular FCC-ee project is also a possible option (see Section IV.2.3). The main advantage is a much higher integrated luminosity; the main limitation is the maximum beam energy (because of synchrotron radiation), that is not sufficient to access the  $ttH$  production mode and the double Higgs production via the  $ZHH$  process. The expected precision for the different machines will be discussed in Section IV.4.4.3.

#### IV.4.4.2 The Higgs boson abundance in 100 TeV proton-proton collisions

In 100 TeV proton-proton collisions, the increase of the Higgs boson production mode cross sections with respect to LHC values is very large (typically a factor 10-20, but up to 50 for  $ttH$ ); Figure 47 (a) shows the dependence of the various production mode cross sections as a function of the centre-of-mass energy. The integrated luminosity possibly collected at the FCC machine could reach  $20 \text{ ab}^{-1}$ ;

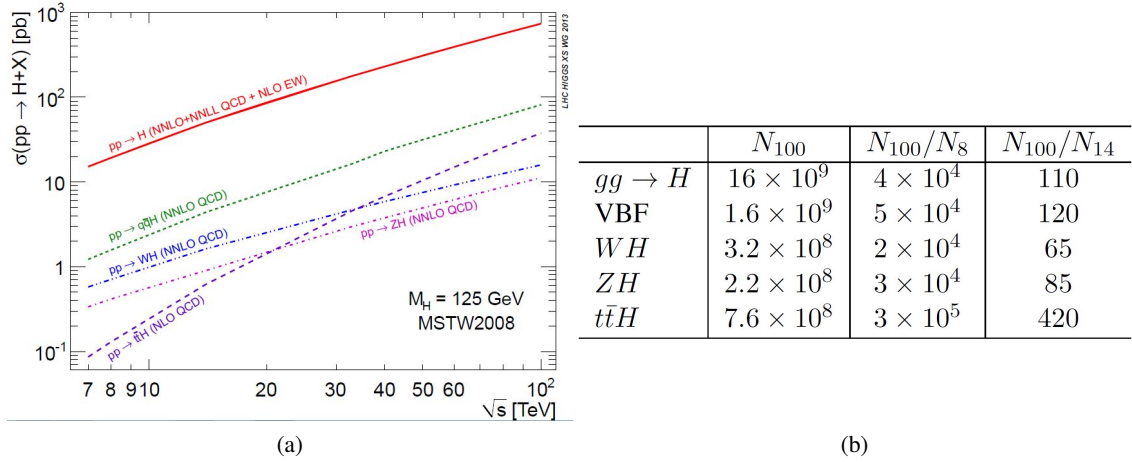


Figure 47: (a) Higgs boson production cross sections as a function of the centre-of-mass energy [6]. (b) Indicative total event rates at 100 TeV ( $N_{100}$ ), and statistical increase with respect to the statistics of LHC Run 1 ( $N_8$ ) and HL-LHC ( $N_{14}$ ), for various production channels [43].

combining both advantages, the statistics increase could exceed a factor 100 (see Figure 47 (b)). In addition, the very high centre-of-mass energy offers a much larger increase for kinematic configurations at large transverse momentum, opening the possibility to explore a completely new dynamic regime. This opportunity is illustrated in two cases:

- Figure 48 (a) shows the integrated Higgs production rates as a function of the minimum Higgs transverse momentum. We can for instance see that  $10^5 H \rightarrow \gamma\gamma$  events are produced at 0.5 TeV (a kinematic region empty in the current LHC datasets);
- Figure 48 (b) illustrates the use of the available statistics for the  $t\bar{t}(H \rightarrow b\bar{b})$  channel in a boosted topology (the Higgs (or  $Z$ ) candidate and the hadronically decaying top candidate are both reconstructed using fat jet techniques). From the measurement of the ratio  $\sigma_{t\bar{t}H}/\sigma_{t\bar{t}Z}$ , an accuracy on the top Yukawa coupling of  $\sim 1\%$  could be accessible [42].

Of course, there is not yet any firm detector design and associated simulation for FCC-pp (while it is the case for ILC); the main goal of the current studies is to build the physics case, exploring what is possible to measure, and to define the detector constraints required to reach the targeted accuracy.

#### IV.4.4.3 Precision comparison

The number of prospect studies on the possible Higgs boson coupling precision reachable at various colliders is colossal. To try to shed some light on this, a comparison has been prepared, based on inputs corresponding to the following scenarios:

- HL-LHC:  $3 \text{ ab}^{-1}$  at 14 TeV [39], [35]
- ILC250:  $2 \text{ ab}^{-1}$  at 250 GeV [44]
- ILC500: mainly  $4 \text{ ab}^{-1}$  at 500 GeV [44]
- FCC-ee: several  $\text{ab}^{-1}$  at 240 GeV [45]

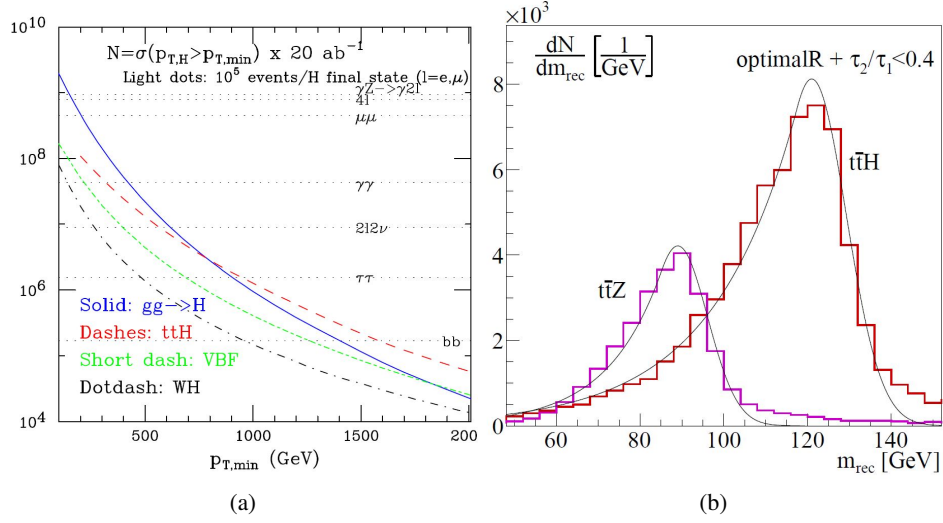


Figure 48: (a) Integrated Higgs boson transverse momentum rates, for various production channels, with  $20 \text{ ab}^{-1}$  [43]. (b) Reconstructed  $m_{bb}$  invariant mass of the Higgs boson and Z boson candidates in a boosted topology [42].

- FCC-hh:  $20 \text{ ab}^{-1}$  at 100 TeV [46].

As mentioned before, a fully model-independent fit is not possible at a hadron collider. In this comparison, the results are presented for a  $\kappa$ -model based on a 7-parameter fit and assuming no exotic Higgs boson decays,  $\kappa_u = \kappa_c = \kappa_t$ ,  $\kappa_d = \kappa_s = \kappa_b$  and  $\kappa_e = \kappa_\mu = \kappa_\tau$ . In a second step, the precision for  $\kappa_{Z\gamma}$  and  $\kappa_\mu$  is computed from the observed corresponding decays, as these decays do not impact the 7-parameter fit given the small SM branching ratios, leading to the determination of 9 parameters. In Table 8 actually appear also  $\kappa_c$  and  $\kappa_e$ , as  $\kappa_c$  can be measured and  $\kappa_e$  can eventually be probed at electron-positron colliders, which gives a total of 11 parameters. The table shows that the main couplings can be measured at the 1% precision or better at ILC or FCC-ee, offering sensitivity to BSM effect in the multi-TeV range in a complementary way to LHC direct searches. One particular case concerns the rare decays ( $\mu\mu$  and  $Z\gamma$ ) and the top coupling, where only the high FCC-hh statistics allows to reach the 1% precision. Of course, to exploit this fantastic potential, experimental and theoretical systematic uncertainties need to be at the same level, which is a real challenge on both sides. In the table, only HL-LHC numbers include some estimated systematic uncertainties.

Parameter	HL-LHC	ILC250	ILC500	FCC-ee	FCC-hh
$\kappa_Z$	4	0.4	0.3	0.15	N.A.
$\kappa_W$	4	1.8	0.4	0.2	N.A.
$\kappa_\gamma$	4	1.1	1.0	1.5	0.5
$\kappa_b$	6	1.8	0.6	0.4	N.A.
$\kappa_t$	8	-	9	-	1
$\kappa_\tau$	6	1.9	0.8	0.5	N.A.
$\kappa_g$	4	2.2	1.0	0.8	N.A.
$\kappa_\mu$	15	5.6	5.1	6.2	1
$\kappa_{Z\gamma}$	25	16	16	N.A.	1
$\kappa_c$	-	2.4	1.2	0.7	N.A.
$\kappa_e$	-	-	-	<100	N.A.

Table 8: Summary of the best precision (in %) reachable for Higgs boson couplings at various facilities. ‘N.A.’ means that the number is ‘Not available’, while ‘-’ means that the coupling is not accessible.

## **Conclusion**

As a final word, I just would like to underline what makes for me our field of experimental particle physics over accelerator at the energy frontier so fascinating: the incredibly complex and long chain from the machine and detector design to discoveries, theoretically expected or not. Huge conceptual and technology challenges, both on the machine side and on the detector side, will have to be overcome in the future to try to deeply progress in our understanding of matter; I am delighted to be a member of this ambitious scientific adventure and to continue my research activities in this field over the next decades.

## References

- [1] V. M. Abazov et al., *Jet energy scale determination in the D0 experiment*, *Nucl. Instrum. Meth.* **A763** (2014) 442, arXiv: 1312.6873 [hep-ex].
- [2] V. M. Abazov et al., *Search for the standard model Higgs boson in the  $ZH \rightarrow \nu\bar{\nu}b\bar{b}$  channel in  $9.5\text{ fb}^{-1}$  of  $p\bar{p}$  collisions at  $\sqrt{s} = 1.96\text{ TeV}$* , *Phys. Lett.* **B716** (2012) 285, arXiv: 1207.5689 [hep-ex].
- [3] G. Aad et al., *Electron reconstruction and identification efficiency measurements with the ATLAS detector using the 2011 LHC proton-proton collision data*, *Eur. Phys. J.* **C74** (2014) 2941, arXiv: 1404.2240 [hep-ex].
- [4] G. Aad et al., *Measurement of the Higgs boson mass from the  $H \rightarrow \gamma\gamma$  and  $H \rightarrow ZZ^* \rightarrow 4\ell$  channels with the ATLAS detector using  $25\text{ fb}^{-1}$  of  $pp$  collision data*, *Phys. Rev.* **D90** (2014) 052004, arXiv: 1406.3827 [hep-ex].
- [5] M. Aaboud et al., *Search for resonances in diphoton events at  $\sqrt{s}=13\text{ TeV}$  with the ATLAS detector*, *JHEP* **09** (2016) 001, arXiv: 1606.03833 [hep-ex].
- [6] LHC Higgs Cross Section Working Group (D. de Florian et al.), *Handbook of LHC Higgs Cross Sections: 4. Deciphering the Nature of the Higgs Sector*, (2016), arXiv: 1610.07922 [hep-ph].
- [7] LHC Higgs Cross Section Working Group (S. Heinemeyer et al.), *Handbook of LHC Higgs Cross Sections: 3. Higgs Properties*, (2013), arXiv: 1307.1347 [hep-ph].
- [8] M. Aaboud et al., *Evidence for the  $H \rightarrow b\bar{b}$  decay with the ATLAS detector*, *JHEP* **12** (2017) 024, arXiv: 1708.03299 [hep-ex].
- [9] A. M. Sirunyan et al., *Evidence for the Higgs boson decay to a bottom quark-antiquark pair*, (2017), arXiv: 1709.07497 [hep-ex].
- [10] M. Aaboud et al., *Evidence for the associated production of the Higgs boson and a top quark pair with the ATLAS detector*, Submitted to: *Phys. Rev. D* (2017), arXiv: 1712.08891 [hep-ex].
- [11] A. M. Sirunyan et al., ‘Evidence for associated production of a Higgs boson with a top quark pair in final states with electrons, muons, and hadronically decaying  $\tau$  leptons at  $\sqrt{s} = 13\text{ TeV}$ ’, tech. rep. CMS-HIG-17-018. CMS-HIG-17-018-003, \* Temporary entry \*: CERN, 2018, URL: <http://cds.cern.ch/record/2308650>.
- [12] ATLAS and CMS Collaborations, *Measurements of the Higgs boson production and decay rates and constraints on its couplings from a combined ATLAS and CMS analysis of the LHC  $pp$  collision data at  $\sqrt{s} = 7$  and  $8\text{ TeV}$* , *JHEP* **08** (2016) 045, arXiv: 1606.02266 [hep-ex].
- [13] ATLAS Collaboration, *The ATLAS Experiment at the CERN Large Hadron Collider*, *JINST* **3** (2008) S08003.
- [14] ATLAS Collaboration, *ATLAS Insertable B-Layer Technical Design Report*, ATLAS-TDR-19 (2010), URL: <https://cds.cern.ch/record/1291633>.

- [15] ATLAS Collaboration, *Performance of the ATLAS trigger system in 2015*, *Eur. Phys. J. C* **77** (2017) 317, arXiv: 1611.09661 [hep-ex].
- [16] GEANT4 Collaboration, *GEANT4: a simulation toolkit*, *Nucl. Instrum. Meth. A* **506** (2003) 250.
- [17] Worldwide LHC Computing group, *Update of the Computing Models of the WLCG and the LHC Experiments*, LCG-TDR-002 (2014), URL: <https://cds.cern.ch/record/1695401>.
- [18] J. Catmore and al., *A new petabyte-scale data derivation framework for ATLAS*, *J. Phys.: Conf. Ser.* **664** (2015) 072007.
- [19] H. Abreu et al., *Performance of the electronic readout of the ATLAS liquid argon calorimeters*, *JINST* **5** (2010) P09003, URL: <http://stacks.iop.org/1748-0221/5/i=09/a=P09003>.
- [20] W. E. Cleland and E. G. Stern, *Signal processing considerations for liquid ionization calorimeters in a high rate environment*, *Nucl. Inst. Methods* **A338** (1994) 467.
- [21] ATLAS Collaboration, *Electron and photon energy calibration with the ATLAS detector using data collected in 2015 at  $\sqrt{s} = 13$  TeV*, ATL-PHYS-PUB-2016-015 (2016), URL: <https://cds.cern.ch/record/2203514>.
- [22] ATLAS Collaboration, *Electron and photon energy calibration with the ATLAS detector using LHC Run 1 data*, *Eur. Phys. J. C* **74** (2014) 3071, arXiv: 1407.5063 [hep-ex].
- [23] K. Grevtsov, *Exploring the diphoton final state at the LHC at 13 TeV: searches for new particles, and the Higgs boson mass measurement with the ATLAS detector*, URL: <https://cds.cern.ch/record/2282674>.
- [24] M. Aaboud et al., *Measurements of Higgs boson properties in the diphoton decay channel with  $36\text{ fb}^{-1}$  of  $pp$  collision data at  $\sqrt{s} = 13$  TeV with the ATLAS detector*, (2018), arXiv: 1802.04146 [hep-ex].
- [25] ATLAS Collaboration, *Measurement of the isolated di-photon cross-section in  $pp$  collisions at  $\sqrt{s} = 7$  TeV with the ATLAS detector*, *Phys. Rev. D* **85** (2012) 012003, arXiv: 1107.0581 [hep-ex].
- [26] ATLAS Collaboration, *Measurement of Higgs boson production in the diphoton decay channel in  $pp$  collisions at center-of-mass energies of 7 and 8 TeV with the ATLAS detector*, *Phys. Rev. D* **90** (2014) 112015, arXiv: 1408.7084 [hep-ex].
- [27] A. Buckley et al., *Rivet user manual*, *Comput. Phys. Commun.* **184** (2013) 2803, arXiv: 1003.0694 [hep-ph].
- [28] G. Aarons et al., *ILC Reference Design Report Volume 1 - Executive Summary*, (2007), ed. by J. Brau, Y. Okada and N. Walker, arXiv: 0712.1950 [physics.acc-ph].
- [29] M. Benedikt, *Future Circular Collider Study Status Overview (FCC Physics Workshop, 11 January 2018)*.
- [30] M. C. Aleksa et al., 'ATLAS Liquid Argon Calorimeter Phase-I Upgrade Technical Design Report', tech. rep. CERN-LHCC-2013-017. ATLAS-TDR-022, Final version presented to December 2013 LHCC., 2013, URL: <https://cds.cern.ch/record/1602230>.

- [31] The ATLAS Collaboration,  
*ATLAS Liquid Argon Calorimeter Phase-II Upgrade Technical Design Report (in preparation)*.
- [32] H. Abramowicz et al.,  
*The International Linear Collider Technical Design Report - Volume 4: Detectors*,  
(2013), ed. by T. Behnke et al., arXiv: [1306.6329 \[physics.ins-det\]](#).
- [33] A. Zaborowska,  
*Design and Performance of electromagnetic for FCC-hh experiment (CHEF Conference 2017)*.
- [34] T. Price, *Digital Electromagnetic Calorimetry at FCC-hh (FCC Week 2017)*.
- [35] S. Dawson et al., ‘Working Group Report: Higgs Boson’,  
*Proceedings, 2013 Community Summer Study on the Future of U.S. Particle Physics: Snowmass on the Mississippi (CSS2013): Minneapolis, MN, USA, July 29-August 6, 2013*,  
2013, arXiv: [1310.8361 \[hep-ex\]](#),  
URL: <https://inspirehep.net/record/1262795/files/arXiv:1310.8361.pdf>.
- [36] M. Delmastro et al., *ANR Photon Portal (<http://lappweb.in2p3.fr/photonportal>)*.
- [37] E. Gabrielli, M. Heikinheimo, B. Mele and M. Raidal,  
*Dark photons and resonant monophoton signatures in Higgs boson decays at the LHC*,  
*Phys. Rev. D* **90** (2014) 055032, arXiv: [1405.5196 \[hep-ph\]](#).
- [38] S. Biswas, E. Gabrielli, M. Heikinheimo and B. Mele,  
*Dark-Photon searches via Higgs-boson production at the LHC*,  
*Phys. Rev. D* **93** (2016) 093011, arXiv: [1603.01377 \[hep-ph\]](#).
- [39] ATLAS Collaboration, *Projections for measurements of Higgs boson signal strengths and coupling parameters with the ATLAS detector at the HL-LHC*,  
ATL-PHYS-PUB-2014-016 (2014), URL: <http://cdsweb.cern.ch/record/1956710>.
- [40] G. Aarons et al.,  
*International Linear Collider Reference Design Report Volume 2: Physics at the ILC*,  
(2007), ed. by A. Djouadi et al., arXiv: [0709.1893 \[hep-ph\]](#).
- [41] J. Yan et al., *Measurement of the Higgs boson mass and  $e^+e^- \rightarrow ZH$  cross section using  $Z \rightarrow \mu^+\mu^-$  and  $Z \rightarrow e^+e^-$  at the ILC*, *Phys. Rev. D* **94** (2016) 113002,  
arXiv: [1604.07524 \[hep-ex\]](#).
- [42] M. L. Mangano, T. Plehn, P. Reimitz, T. Schell and H.-S. Shao,  
*Measuring the Top Yukawa Coupling at 100 TeV*, *J. Phys. G* **43** (2016) 035001,  
arXiv: [1507.08169 \[hep-ph\]](#).
- [43] R. Contino et al., *Physics at a 100 TeV pp collider: Higgs and EW symmetry breaking studies*,  
*CERN Yellow Report* (2017) 255, arXiv: [1606.09408 \[hep-ph\]](#).
- [44] K. Fujii et al., *Physics Case for the 250 GeV Stage of the International Linear Collider*, (2017),  
arXiv: [1710.07621 \[hep-ex\]](#).
- [45] D. d’Enterria, ‘Physics at the FCC-ee’, *Proceedings, 17th Lomonosov Conference on Elementary Particle Physics: Moscow, Russia, August 20-26, 2015*, 2017 182,  
arXiv: [1602.05043 \[hep-ex\]](#),  
URL: <https://inspirehep.net/record/1421932/files/arXiv:1602.05043.pdf>.
- [46] M. Mangano et al., *Physics at its limits (<http://cerncourier.com/cws/article/cern/68433>)*.

# Appendix

## A Other contributions

In this appendix are listed my other main contributions (with the list of relevant publications) from my post-PhD period but which are not discussed in this report.

### A.1 D0 experiment

- Calibration of the jet energy scale, using the Jet Smearing Shifting and Removing method

Publication:

- *Jet energy scale determination in the D0 experiment*  
D0 Collaboration, V. M. Abazov et al.,  
Nucl. Instrum. Methods in Phys. Res. Sect. A, Volume 763, 1 November 2014, Pages 44275,  
arXiv:1312.6873 [hep-ex]

- Search for a low mass Higgs boson in the  $ZH \rightarrow \nu\bar{\nu}b\bar{b}$  channel

Publications:

- *Search for the standard model Higgs boson in the  $ZH \rightarrow \nu\bar{\nu}b\bar{b}$  channel in  $9.5\text{ fb}^{-1}$  of  $p\bar{p}$  collisions at  $\sqrt{s} = 1.96\text{ TeV}$*   
D0 Collaboration, V. M. Abazov et al.,  
Phys.Lett. B716 (2012) 28593,  
arXiv:1207.5689 [hep-ex]
- *Combined search for the standard model Higgs boson decaying to  $bb$  using the D0 Run II dataset*  
D0 Collaboration, V. M. Abazov et al.,  
Phys.Rev.Lett. 109 (2012) 121802,  
arXiv:1207.6631 [hep-ex]
- *Evidence for a particle produced in association with weak bosons and decaying to a bottom-antibottom quark pair in Higgs boson searches at the Tevatron*  
CDF Collaboration, D0 Collaboration, T. Aaltonen et al.,  
Phys.Rev.Lett. 109 (2012) 071804,  
arXiv:1207.6436 [hep-ex]

### A.2 ATLAS experiment

- Measurement of electron identification efficiencies at Run 1

Publication:

- *Electron reconstruction and identification efficiency measurements with the ATLAS detector using the 2011 LHC proton-proton collision data*  
ATLAS Collaboration (Aad, Georges et al.)  
Eur.Phys.J. C74 (2014) 2941  
arXiv:1404.2240 [hep-ex]

- Measurement of the Higgs boson properties in the  $H \rightarrow ZZ^* \rightarrow 4l$  channel at Run 1

Publications:

- *Measurement of the Higgs boson mass from the  $H \rightarrow \gamma\gamma$  and  $H \rightarrow ZZ^* \rightarrow 4l$  channels with the ATLAS detector using 25 fb<sup>-1</sup> of pp collision data*  
ATLAS Collaboration, G. Aad et al.,  
Phys.Rev. D90 (2014) 052004,  
arXiv:1406.3827 [hep-ex]
- *Measurements of Higgs boson production and couplings in the four-lepton channel in pp collisions at center-of-mass energies of 7 and 8 TeV with the ATLAS detector*  
ATLAS Collaboration, G. Aad et al.,  
Phys.Rev. D91 (2015) 012006,  
arXiv:1408.5191 [hep-ex]

- Search for a high mass resonance in the diphoton channel (also known as the '750 GeV excess')

Publication:

- *Search for resonances in diphoton events at 13 TeV with the ATLAS detector*  
The ATLAS collaboration, Aaboud, M., Aad, G. et al.  
J. High Energ. Phys. (2016) 2016: 1. doi:10.1007/JHEP09(2016)001